Euclid Quick Data Release (Q1)

The *Euclid* view on *Planck* galaxy protocluster candidates: towards a probe of the highest sites of star formation at cosmic noon

Euclid Collaboration: T. Dusserre[1], H. Dole[⋆,1], F. Sarron[2,3], G. Castignani[4], N. Ramos-Chernenko[5,6], N. Aghanim[1], A. Garic[1], I.-E. Mellouki[1], N. Dagoneau[7], O. Chapuis[8], B. L. Frye[9], M. Polletta[10,11], H. Dannerbauer[6], M. Langer[1], L. Maurin[1], E. Soubrie[1], A. Biviano[12,13], N. Mai[86,87], S. Mei[86,87], B. Altieri[14], A. Amara[15], S. Andreon[16], N. Auricchio[4], C. Baccigalupi[13,12,17,18], M. Baldi[19,4,20], A. Balestra[21], S. Bardelli[4], P. Battaglia[4], A. Bonchi[22], D. Bonino[23], E. Branchini[24,25,16], M. Brescia[26,27], J. Brinchmann[28,29], S. Camera[30,31,23], V. Capobianco[23], C. Carbone[10], J. Carretero[32,33], S. Casas[34], M. Castellano[35], S. Cavuoti[27,36], K. C. Chambers[37], A. Cimatti[38], C. Colodro-Conde[5], G. Congedo[39], C. J. Conselice[40], L. Conversi[41,14], Y. Copin[42], A. Costille[43], F. Courbin[44,45], H. M. Courtois[46], M. Cropper[47], A. Da Silva[48,49], H. Degaudenzi[50], G. De Lucia[12], A. M. Di Giorgio[51], C. Dolding[47], F. Dubath[50], C. A. J. Duncan[40], X. Dupac[14], S. Dusini[52], S. Ealet[42], S. Escoffier[53], M. Farina[51], R. Farinelli[4], F. Faustini[22,35], S. Ferriol[42], F. Finelli[4,54], P. Fosalba[55,56], S. Fotopoulou[57], M. Frailis[12], E. Franceschi[4], M. Fumana[10], S. Galeotta[12], K. George[58], B. Gillis[39], C. Giocoli[4,20], P. Gómez-Alvarez[59,14], J. Gracia-Carpio[60], A. Grazian[21], F. Grupp[60,58], L. Guzzo[61,16,62], S. Gwyn[63], S. V. H. Haugan[64], J. Hoar[14], W. Holmes[65], F. Hormuth[66], A. Hornstrup[67,68], P. Hudelot[69], K. Jahnke[70], M. Jhabvala[71], E. Keihänen[72], S. Kermiche[53], A. Kiessling[65], B. Kubik[42], K. Kuijken[73], M. Kümmel[58], M. Kunz[74], H. Kurki-Suonio[75,76], Q. Le Boulc'h[77], A. M. C. Le Brun[78], D. Le Mignant[43], S. Ligori[23], P. B. Lilje[64], V. Lindholm[75,76], I. Lloro[79], G. Mainetti[77], D. Maino[61,10,62], E. Maiorano[4], O. Mansutti[12], S. Marcin[80], O. Marggraf[81], M. Martinelli[35,82], N. Martinet[43], F. Marulli[83,4,20], R. Massey[84], S. Maurogordato[85], E. Medinaceli[4], M. Melchior[88], Y. Mellier[89,69], E. Meneghetti[4,20], E. Merlin[35], G. Meylan[90], A. Mora[91], M. Moresco[83,4], L. Moscardini[83,4,20], C. Neissner[92,33], R. C. Nichol[15], S.-M. Niemi[93], J. W. Nightingale[94], C. Padilla[92], S. Paltani[50], F. Pasian[12], K. Pedersen[95], W. J. Percival[96,97,98], V. Pettorino[93], S. Pires[99], G. Polenta[22], M. Poncet[100], L. A. Popa[101], L. Pozzetti[4], F. Raison[60], R. Rebolo[5,102,103], A. Renzi[104,52], J. Rhodes[65], G. Riccio[27], E. Romelli[12], M. Roncarelli[4], R. Saglia[58,60], Z. Sakr[105,106,107], A. G. Sánchez[60], D. Sapone[108], B. Sartoris[58,12], M. Schirmer[70], P. Schneider[81], T. Schrabback[109], A. Secroun[53], G. Seidel[70], S. Serrano[55,110,56], P. Simon[81], C. Sirignano[104,52], G. Sirri[20], L. Stanco[52], J. Steinwagner[60], P. Tallada-Crespí[32,33], A. N. Taylor[39], H. I. Teplitz[111], I. Tereno[48,112], S. Toft[113,114], R. Toledo-Moreo[115], F. Torradeflot[33,32], I. Tutusaus[106], L. Valenziano[4,54], J. Valiviita[75,76], T. Vassallo[58,12], G. Verdoes Kleijn[116], A. Veropalumbo[16,25,24], Y. Wang[111], J. Weller[58,60], A. Zacchei[12,13], G. Zamorani[4], F. M. Zerbi[16], I. A. Zinchenko[58], E. Zucca[4], V. Allevato[27], M. Ballardini[117,118,4], M. Bolzonella[4], E. Bozzo[50], C. Burigana[119,54], R. Cabanac[106], A. Cappi[4,85], D. Di Ferdinando[20], J. A. Escartin Vigo[60], G. Fabbian[120], L. Gabarra[121], M. Huertas-Company[5,6,122,123], J. Martín-Fleitas[91], S. Matthew[39], M. Maturi[105,124], N. Mauri[38,20], R. B. Metcalf[83,4], A. Pezzotta[125,60], M. Pöntinen[75], C. Porciani[81], I. Risso[126], V. Scottez[89,127], M. Sereno[4,20], M. Tenti[20], M. Viel[13,12,18,17,128], M. Wiesmann[64], Y. Akrami[129,130], S. Alvi[117], I. T. Andika[131,132], S. Anselmi[52,104,133], M. Archidiacono[61,62], F. Atrio-Barandela[134], K. Benson[47], P. Bergamini[61,4], D. Bertacca[104,21,52], M. Bethermin[135], A. Blanchard[106], L. Blot[136,133], H. Böhringer[60,137,138], S. Borgani[139,13,12,17,128], M. L. Brown[40], S. Bruton[140], A. Calabro[35], B. Camacho Quevedo[55,56], F. Caro[35], C. S. Carvalho[112], T. Castro[12,17,13,128], F. Cogato[83,4], T. Contini[106], A. R. Cooray[141], M. Costanzi[139,12,13], O. Cucciati[4], S. Davini[25], F. De Paolis[142,143,144], G. Desprez[116], A. Díaz-Sánchez[145], J. J. Diaz[6,5], S. Di Domizio[24,25], J. M. Diego[146], P.-A. Duc[135], A. Enia[19,4], Y. Fang[58], A. G. Ferrari[20], P. G. Ferreira[121], A. Finoguenov[75], A. Franco[143,142,144], K. Ganga[86], J. García-Bellido[129], T. Gasparetto[12], V. Gautard[147], E. Gaztanaga[56,55,148], F. Giacomini[20], F. Gianotti[4], A. H. Gonzalez[149], G. Gozaliasl[150,75], A. Gruppuso[4,20], M. Guidi[19,4], C. M. Gutierrez[151], A. Hall[39], W. G. Hartley[50], S. Hemmati[152], C. Hernández-Monteagudo[103,5], H. Hildebrandt[153], J. Hjorth[95], J. J. E. Kajava[154,155], Y. Kang[50], V. Kansal[156,157], D. Karagiannis[117,158], K. Kiiveri[72], C. C. Kirkpatrick[72], S. Kruk[14], J. Le Graet[53], L. Legrand[159,160], M. Lembo[117,118], F. Lepori[161], G. Leroy[162,84], G. F. Lesci[83,4], J. Lesgourgues[34], L. Leuzzi[83,4], T. I. Liaudat[163], S. J. Liu[51], A. Loureiro[164,165], J. Macias-Perez[166], G. Maggio[12], M. Magliocchetti[51], E. A. Magnier[37], F. Mannucci[167], R. Maoli[168,35], C. J. A. P. Martins[169,28], M. Migliaccio[170,171], M. Miluzio[14,172], P. Monaco[139,12,17,13], C. Moretti[18,128,12,13,17], G. Morgante[4], S. Nadathur[148], K. Naidoo[148], A. Navarro-Alsina[81], S. Nesseris[129],

F. Passalacqua[104, 52], K. Paterson[70], L. Patrizii[20], A. Philippon[1], A. Pisani[53, 173], D. Potter[161], S. Quai[83, 4], M. Radovich[21], G. Rodighiero[104, 21], S. Sacquegna[142, 143, 144], M. Sahlén[174], D. B. Sanders[37], E. Sarpa[18, 128, 17], A. Schneider[161], D. Sciotti[35, 82], E. Sellentin[175, 73], F. Shankar[176], L. C. Smith[177], S. A. Stanford[178], K. Tanidis[121], G. Testera[25], R. Teyssier[173], S. Tosi[24, 126], A. Troja[104, 52], M. Tucci[50], C. Valieri[20], A. Venhola[179], D. Vergani[4], G. Verza[180], P. Vielzeuf[53], N. A. Walton[177], J. R. Weaver[181], J. G. Sorce[182, 1], and D. Scott[183]

(Affiliations can be found after the references)

March 28, 2025

ABSTRACT

We search for galaxy protoclusters at redshifts $z > 1.5$ in the first data release (Q1) of the *Euclid* survey. We make use of the catalogues delivered by the *Euclid* Science Ground Segment (SGS), especially the positions, photometry, photometric redshifts, and derived physical parameters. After a galaxy selection on the H_E magnitude and on the photometric redshift quality, we undertake the search using the DETECTIFz algorithm, an overdensity finder based on Delaunay tessellation that uses photometric redshift probability distributions through Monte Carlo simulations. In this pilot study, we conduct a search in the 11 *Euclid* tiles that contain previously known *Planck* high star-forming galaxy protocluster candidates, covering $2.75 \deg^2$ of the whole $63 \deg^2$ of Q1. We then focus on the two *Euclid* protocluster candidates that coincide with these *Planck* fields. These counterparts lie at photometric redshifts $z_{ph} = 1.63^{+0.19}_{-0.23}$ and $z_{ph} = 1.56^{+0.18}_{-0.21}$. One of them also has partial *Herschel* coverage. Both detections have been confirmed by the independent protocluster detection algorithms Poisson Probability Method (PPM) and Monte-Carlo Delaunay Tesselation Field Estimator (MC-DTFE-LoG). We study the colours, the derived stellar masses (regarded as lower limits) and star-formation rates of the detected protoclusters. We also estimate their halo mass lower limits using stellar mass-halo mass relations from the literature. We investigate whether we are intercepting these galaxy overdensities in their 'dying' (or 'swan song') phase, such that the high star-formation rates would be due to their last unsustainable starburst (or star-formation event) before transitioning and maturing to groups or clusters of galaxies. Some galaxy members are found to lie above the main sequence of galaxies (star-formation rate versus stellar mass). These *Planck* and *Euclid* overdense regions occupy a position in the dark matter halo mass (M_h) / redshift (z) plane at $13.0 < \log_{10} M_h < 13.5$, $1.5 < z < 2$; in this locus, halos of forming galaxy clusters are expected to have experienced a transition between cold flows with no shock heating throughout the halo to shock heating in the halo. Finally, we empirically update the potential for galaxy protocluster discoveries at redshift up to $z \simeq 3$ (wide survey) and $z \simeq 5.5$ (deep survey) with *Euclid* for the next data release (DR1).

Key words. Methods: statistical – Surveys – Cosmology: observations – large-scale structure of Universe – Galaxies: clusters: general – Galaxies: star formation

1. Introduction

Large-scale structure in the Universe forms hierarchically via the gravitational collapse of initial density perturbations. This is distributed in the form of a complex cosmic web network of filaments, walls, voids, and nodes. The most massive nodes, at the intersection of filaments, are the sites of clusters of galaxies and of their high-redshift progenitors, usually called 'protoclusters' (e.g., Overzier 2016; Alberts & Noble 2022; Remus et al. 2023). Understanding how the present largest gravitationally bound structures, namely clusters of galaxies, transitioned from an early protocluster stage, is a key question in the process of matter assembly in the Universe.

The most common definition for a protocluster is an overdensity in the matter field that should reach a virial mass of at least $10^{14} M_\odot$ at $z = 0$ under the spherical collapse model (Chiang et al. 2013; Muldrew et al. 2015; Overzier 2016; Chiang et al. 2017; Alberts & Noble 2022; Remus et al. 2023). Although this definition is relevant when dealing with simulations, it is more difficult to use with observational data. Indeed, protoclusters have mainly been detected as galaxy overdensities; however, in their final state, their most massive parts are the dark matter halo mass ($80-85\%$) and the intracluster medium ($10-12\%$). Although both of these masses are linked by assuming virialisation, the intracluster medium in protoclusters is cooler by several orders of magnitudes than what is needed for current instruments to detect it. Another solution to measure their masses would be to pick galaxy overdensities that act as gravitational lenses, but this would restrict us to only study a handful of candidates. Therefore, instead of the mass-based definition, we follow Gouin et al. (2022), who found from simulations that there

is a 92% chance that a structure composed of at least seven gravitationally bound star-forming galaxies is a protocluster. Earlier works (Casey 2016) reached similar conclusions based on the observation of dusty star-forming galaxies.

Protoclusters are pivotal for understanding structure formation because they represent the environments primarily driving the properties of their descendant clusters, both in terms of the mechanisms controlling the evolution of galaxy members and in terms of the gas-heating processes (see Alberts & Noble 2022, for a recent review). In this context, a particularly crucial, but still not understood mechanism, is quenching (Martig et al. 2009; Schawinski et al. 2014), which describes the transition from star-forming to quiescent galaxies. It marks the end of the so-called Cosmic Noon, at $z \simeq 1.5$–3, which represents the peak epoch for the formation of galaxies and their assembly into clusters (Madau & Dickinson 2014). As such, protoclusters seem to be among the best witnesses of this transition and their observation in the submillimetre (submm) and infrared (IR) domains offers great opportunities not only to detect them, but also to study star formation and quenching processes at Cosmic Noon. Based on the assumption that important episodes of star formation occurred in protoclusters, several approaches have been proposed to capture this epoch, such as the search for overdensities of Hα and Lyα emitters (Steidel et al. 2000; Shi et al. 2019; Koyama et al. 2013) or of dusty star-forming galaxies and submm galaxies (Chapman et al. 2009; Clements et al. 2014; Kubo et al. 2015; Casey et al. 2015; Wang et al. 2016; Miller et al. 2018; Gómez-Guijarro et al. 2018; Coogan et al. 2018; Oteo et al. 2018; Kneissl et al. 2019; Tadaki et al. 2019; Emonts et al. 2019; Koyama et al. 2021; Polletta et al. 2021; Calvi et al. 2021; Rotermund et al. 2021; Hill et al. 2024).

Table 1. The 12 *Planck* protocluster candidates located in the *Euclid* Q1 footprint (Euclid Collaboration: Aussel et al. 2025; Euclid Quick Release Q1 2025), in 11 tiles.

Euclid field	*Planck* source	*Planck* ID	RA	Dec	MER tile
EDF-F	G221.09−54.59[a]	1904	52.6798	−26.4142	102 046 112
EDF-F	G222.05−54.24[a]	1399	53.1806	−26.9014	102 045 467
EDF-F	G222.75−55.98[a]	108	51.3123	−27.5725	102 044 821
EDF-F	G223.18−54.86[a]	2151	52.6060	−27.6495	102 044 824
EDF-F	G224.36−53.19[a]	1643	54.5941	−28.0819	102 044 188
EDF-S	G257.45−49.50	320	57.4918	−48.7670	102 020 530
EDF-S	G252.47−48.60	600	59.8577	−45.7809	102 023 474
EDF-S	G254.74−47.64[a]	1308	60.8251	−47.4485	102 021 984
EDF-S	G257.13−49.16	1442	58.0698	−48.6542	102 021 010
EDF-S	G254.49−47.73	1494	60.7380	−47.2715	102 021 984
EDF-S	G257.71−47.99	1926	59.6462	−49.3164	102 020 059
EDF-S	G257.01−45.18	1975	64.0252	−49.4534	102 020 065

Notes. [a] *Herschel*/SPIRE observations are available and come from Oliver et al. (2012) in EDF-F and Planck Collaboration (2015b) in EDF-S. Columns are: *Euclid* field name; *Planck* field name; *Planck* ID (in the high-z source candidate catalogue of Planck Collaboration 2016, and available on the *Planck* Legacy Archive at ESA); RA and Dec in degrees for the *Planck* source; and the *Euclid* MER tile number (Euclid Collaboration: Romelli et al. 2025). Notice that two of the *Planck* sources fall in the same *Euclid* tile.

In the same spirit, the largest catalogue of candidate protoclusters contains 2151 high-redshift sources over 28% of the sky (Planck Collaboration 2016), performed by *Planck*.[1] This was complemented by 228 deep *Herschel*/SPIRE[2] observations described in Planck Collaboration (2015b), but only 91 of these *Planck* sources ended-up in the final *Planck* catalogue. Approximately 100 follow-up observations in the near-IR (NIR) were also performed with *Spitzer*[3] (Martinache et al. 2018). Gouin et al. (2022) used the IllustrisTNG simulations (Pillepich et al. 2018; Nelson et al. 2019) to reproduce the *Planck* selection; they confirmed the contamination of star-forming sources along the line of sight, but they also showed that more than 70% of the *Planck* protocluster candidates are expected to evolve into galaxy clusters by $z = 0$, by the definition that seven galaxies are in (projected) close proximity. The *Planck* protocluster candidates (Planck Collaboration 2016) were selected by colour in the High-Frequency Instrument (HFI) submm-cleaned images, targeting $z \simeq 2$ groups of rest-fram far-IR galaxies having significant star-formation activity. This sample is thus different from the Sunyaev-Zeldovich (SZ) cluster catalogue (Planck Collaboration 2015a). We refer the reader to Planck Collaboration (2016) for details on the construction of the *Planck* catalogue of protocluster candidates.[4] Follow-up observations and physical characterisation of some candidates were also performed (Flores-Cacho et al. 2016; Negrello et al. 2017; Martinache et al. 2018; Polletta et al. 2021, 2022; Hill et al. 2024), including with the James Webb Space Telescope (Polletta et al. 2024) .

Following the first discoveries of high-redshift clusters and protoclusters during the last few decades (Euclid Collaboration: Böhringer et al. 2025, and references on protocluster detections therein), an increasingly large number of protoclusters have been detected, significantly enriching the samples of sources needed to decipher the steps by which clusters grow, assemble matter, and shape the properties of their member galaxies across time.

Detection and follow-up confirmation of protoclusters have been conducted in many wavebands from the radio to the optical.

Given their rarity, the number of protoclusters is still small and it is only via large surveys conducted at these wavelengths that the observational situation is expected to drastically change. The large number of candidate protoclusters detected by *Planck* (Planck Collaboration 2016) illustrates the advantage of surveying the whole sky to increase the source statistics, with the caveat that one has to use appropriate physical tracers and detection techniques of protoclusters in order to reduce contamination by false detections. In this context, stage III (Albrecht et al. 2006) wide galaxy surveys, such as the Hyper Suprime-Cam Strategic Survey Program (Aihara et al. 2018), already show that blind detection of more than 100 protocluster candidates at $z \simeq 4$ is possible. Undoubtedly, stage IV surveys, such as *Euclid* (Euclid Collaboration: Mellier et al. 2024), Rubin/LSST[5], or *Roman*[6], covering about a third of the sky, will offer unique possibilities to observe high-redshift galaxies and identify tens of thousands of overdense regions that could be associated with distant clusters and/or protoclusters (e.g., Euclid Collaboration: Böhringer et al. 2025).

In this study, we showcase the capability of *Euclid* (Euclid Collaboration: Mellier et al. 2024) to detect galaxy protoclusters. We decide to test the galaxy overdensity search algorithms and assess if we can identify with *Euclid* any of the *Planck* high-redshift candidates (Planck Collaboration 2016), in which we expect to find highly star-forming galaxy protoclusters, since they were selected by their rest-frame far-infrared colours. For this reason, we will only be investigating the counterparts in the *Euclid* Q1 data set (Euclid Collaboration: Aussel et al. 2025; Euclid Quick Release Q1 2025) of protocluster candidates already identified with *Planck*. This pilot study hence provides a first assessment of the *Planck-Euclid* synergy to probe star-forming galaxy protoclusters at Cosmic Noon.

Section 2 provides a description of the *Euclid* observations and fields used in the study, in particular the 11 tiles matching the positions of *Planck* sources. In Sect. 3, we describe the methods used to detect galaxy overdensities in the *Euclid* data. In Sect. 4 we highlight the two *Euclid* protocluster detections as counter-

---

[1] *Planck* mission: Planck Collaboration (2020a)
[2] *Herschel*/SPIRE: Griffin et al. (2010)
[3] *Spitzer*: Werner et al. (2004); Soifer et al. (2008)
[4] Called 'PHz' for the *Planck* catalogue of high-z candidates. We shall avoid use of this label here because of confusion with the 'PHZ' (photometric redshifts) of *Euclid*.
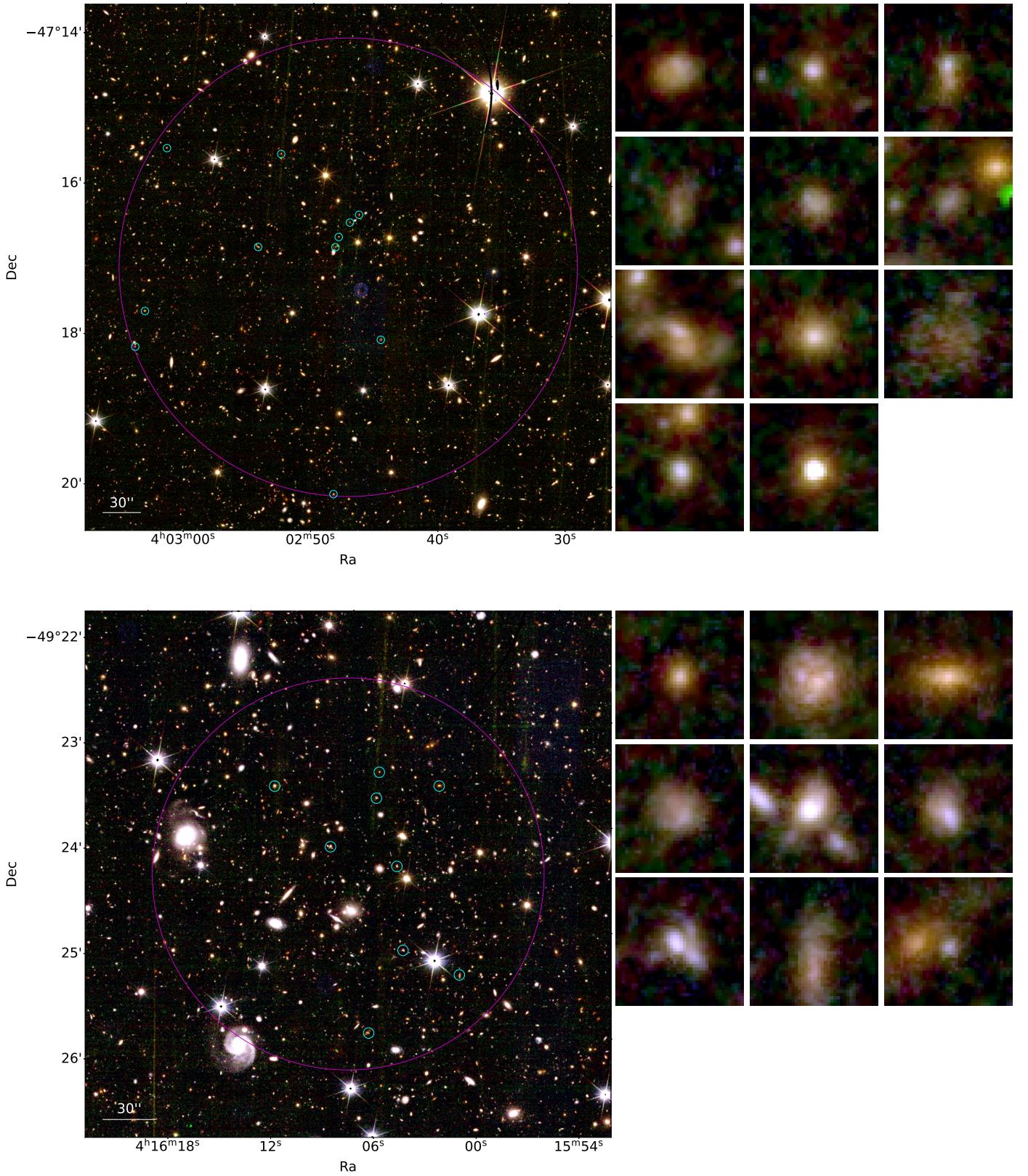
[5] https://rubinobservatory.org
[6] https://roman.gsfc.nasa.gov

Fig. 1. *Euclid* colour images made using VIS $I_{\rm E}$ (blue), NIR $Y_{\rm E}$ (green), and NIR $H_{\rm E}$ (red) images of our two best candidates. *Top left*: The G254_EUC_2 protocluster candidate detected by DETECTIFz at $z_{\rm ph} = 1.63^{+0.19}_{-0.23}$ – north is up, east is to the left, and the image covers $7' \times 7'$. *Bottom left*: The G257_EUC_3 protocluster candidate detected by DETECTIFz at $z_{\rm ph} = 1.56^{+0.18}_{-0.21}$ – north is up, east is to the left, and the image covers $5' \times 5'$. The large purple circles represent the radius of the structure determined by DETECTIFz, and the small cyan circles correspond to galaxies belonging to the structure. Cutouts on the right are centred on galaxies selected as members and cover $4'' \times 4''$.

parts of *Planck* protocluster candidates (shown in Fig. 1), and explore their physical properties in Sect. 5. We discuss our findings in Sect. 6, in particular the level to which our detections match the expectations of protoclusters and their evolutionary states. In Sect. 7 we provide empirical predictions for the redshift range probed by future *Euclid* protocluster detections. Finally, we conclude in Sect. 8 and review what this pilot study raises as open questions. Throughout this paper, we use AB magnitudes, and the *Planck* 2018 flat ΛCDM cosmology (Planck Collaboration 2020a,b) with $H_0 = 67.66\,\mathrm{km\,s^{-1}\,Mpc^{-1}}$, $\Omega_b = 0.0489$, $\Omega_m = 0.3111$, and $\Omega_\Lambda = 0.6889$.

2. *Euclid* observations, data processing, and selected sky areas in the Q1 footprint

2.1. Euclid observations and data processing

Euclid has observed the three Euclid Deep Fields (EDFs), and the Q1 data release (Euclid Collaboration: Aussel et al. 2025) selects the first passes, corresponding to the approximate depth of the Euclid Wide Survey (EWS). Processing is performed by the science ground segment (SGS) from images delivered by the VIS (Euclid Collaboration: Cropper et al. 2024; Euclid Collaboration: McCracken et al. 2025) and NISP instruments (Euclid Collaboration: Jahnke et al. 2024; Euclid Collaboration: Polenta et al. 2025). Here we make use of the multiwavelength photometric catalogue delivered by the 'merged' processing function MER (Euclid Collaboration: Romelli et al. 2025) and the 'photometric redshift' processing function (PF), or PHZ for short (Euclid Collaboration: Tucci et al. 2025). We use the *Euclid* VIS (see Appendix A) and NIR stacked tiles in bands I_E, Y_E, J_E, and H_E delivered by MER, together with the photometric redshift probability distribution function (PDF), and the distributions of magnitudes and colours. The MER photometric catalogue is merged with the PHZ photometric redshift catalogue and the resulting catalogue used as an input for the protocluster detection algorithms.

2.2. Selected sky areas: the 11 Euclid tiles of interest for 12 Planck protocluster candidates

The footprint of the EDF-F and EDF-S Q1 fields are shown in Fig. A.1, together with the *Planck* protocluster candidates of Planck Collaboration (2016). 12 *Planck* protocluster candidates fall in 11 *Euclid* tiles. Table 1 reports the specific *Euclid* MER tile numbers (Euclid Collaboration: Romelli et al. 2025) used in this paper.

3. Protocluster detection algorithms and selection

3.1. Selection for input

Each *Euclid* tile covers $30' \times 30'$ and contains on average 110 000 sources (Euclid Collaboration: Romelli et al. 2025). Uncertainties on photometry and astrometry come from the *Euclid* SGS MER PF (Euclid Collaboration: Romelli et al. 2025). Photometric redshifts (full PDFs), and derived physical parameters (mainly used here are stellar masses and SFRs) are obtained from PHZ (Euclid Collaboration: Tucci et al. 2025).

We select the *Euclid* sources in the MER and PHZ catalogues with the following conditions:

- $H_E < 24$;

- $\delta z_{ph}/(1 + z_{ph}) < 0.10$, with z_{ph} being the median photometric redshift and δz_{ph} the uncertainty (taken at 68% of the PDF, the photo-z PDF), see Sect. 3.2 for a discussion about this threshold;
- sources are relatively isolated from bright stars and/or known remaining artefacts, to account for this we select MER sources with a spurious probability below 20%;
- sources belong to the 11 MER tiles (reported in Table 1).

This provides the input for the protocluster search algorithms.

3.2. DETECTIFz protocluster finding algorithm

With the goal of identifying the counterparts of the *Planck*-detected protocluster candidates, we apply the DETECTIFz (DElaunay TEssellation ClusTer IdentiFication with photo-z) algorithm (Sarron & Conselice 2021) on the 11 *Euclid* tiles containing a *Planck* protocluster candidate. The DETECTIFz algorithm uses the Delaunay Tessellation Field Estimator (DTFE) to identify extended galaxy overdensities within redshift slices. This method is entirely empirical and independent from cosmological models, relying exclusively on galaxy sky coordinates and samples drawn from the photometric redshift probability distribution.

Beginning with a galaxy catalogue containing sky coordinates and photometric redshift probabilities, DETECTIFz constructs a 3D overdensity map. Overdensities are estimated in redshift slices spaced by 0.01 and with varying widths of $\pm 1\,\sigma_z(z)$, derived from the input galaxy catalogue. For each slice, DETECTIFz generates 100 Monte Carlo realisations of the overdensity map by sampling from the photometric redshift probability distribution and applying DTFE to each sample. The final density map is obtained by averaging over these realisations.

If the redshift error is too high, a galaxy will spread over a large redshift range in the 100 Monte Carlo realisations, resulting in a potentially biased estimation of the mean density. That, coupled to the possible systematic effects in photo-z determination over an absolute error $\delta z = 0.1$, motivated our choice to pre-select galaxies by imposing the threshold $\delta z_{ph}/(1 + z_{ph}) < 0.10$. To ensure that our detections were not a result of this selection only, we ran DETECTIFz with the relaxed constraint $\delta z_{ph}/(1 + z_{ph}) < 0.15$ and recovered the same *Planck* counterparts. To avoid biases due to spurious detections, we also make use of the SPURIOUS_PROB column in MER catalogues. Before running DETECTIFz, we cut out every source that has more than 20% probability of being a spurious object.

Within each slice, overdensities are identified as extended peaks in the density map. For each detection, the algorithm records a bounding box (RA_{min}, RA_{max}, Dec_{min}, Dec_{max}) that encloses regions with pixel values above the $(S/N)_{min}$ threshold. To eliminate multiple detections of the same protocluster across adjacent slices or substructures, the algorithm merges peaks that are contiguous along the line of sight (i.e., in the redshift direction) and have either overlapping bounding boxes or peak separations of less than 2 comoving Mpc. These merged regions constitute the final galaxy protocluster candidates.

This selected sample (Sect. 3.1) is used as an input for DETECTIFz, to which we provide celestial coordinates and the full photometric redshift PDF. We force DETECTIFz to search within the redshift range 1.35–3.5, and to only select structures above a S/N of $2\,\sigma$. DETECTIFz produces a list of overdensities and includes S/N, as well as measurements of overdensity and radius (Sarron & Conselice 2021). In DETECTIFz, S/N is

computed for each detection in each slice, within a disc of fixed radius of 500 comoving kpc (R_{500})[7] around the peak. For each slice, we calculate the mean (μ_δ) and standard deviation (σ_δ) of the entire density map, after applying a 3σ-clipping to remove outliers. The mean overdensity signal in the region around the peak is then compared to these global values to form the overall S/N:

$$S/N = \frac{\langle \log(1 + \delta)\rangle_{R_{500}} - \mu_\delta}{\sigma_\delta}.$$ (1)

Using the magnitude, spurious probability, and relative redshift cuts on the *Euclid* catalogue of galaxies, we find a total of 89 'raw' overdensities with S/N > 2 in the 11 *Euclid* tiles.

3.3. Post-selection after DETECTIFz: our sample

From the 89 DETECTIFz detections, we post-select as protocluster candidates the overdensities satisfying simultaneously these conditions:

(a) contain galaxies with more than 68% probability of being a member, and no sign of artefacts due to foreground stars;

(b) have at least seven galaxy members, according to the criterion of Gouin et al. (2022);

(c) have not been contaminated by bright stars, low-redshift interlopers and/or photometric artefacts, despite the cutoff based on the spurious probability.

We have at this stage 10 protoclusters candidates, among which eight have S/N above 3. The photometric redshift distribution of the sample is shown in Fig. 2, and the star-formation rates versus stellar masses (see Sect. 5.2) are plotted in Fig. 3.

We add another criterion for this pilot study:

(d) the angular position falls within one of the 12 *Planck* beams.

Two protocluster candidates fall within a *Planck* beam (that is in a 5′ radius of the central position of the *Planck* detection; Fig. 1). As stated in Sect. 1, we choose to focus on these two *Planck* counterparts from this point on. They are reported in Table 2 and are also shown in Figs. 2 and 3.

3.4. Detections with PPM and MC-DTFE-LoG

We consolidate the detections of *Euclid* counterparts of *Planck* protocluster candidates using two other independent algorithms.

Firstly, we use the Poisson probability method (PPM). The PPM searches for high-z megaparsec-scale overdensities of galaxies around a given target. It is based on a theory defined on the ensemble of the photometric redshift realisations of the galaxies in the field. Through the use of a solid positional prior and an accurate photometric redshift sampling, PPM partially overcomes the limitations deriving from low number-count statistics and shot-noise fluctuations, which are particularly relevant in the high-z Universe, such as in the case of protoclusters. More specifically, the PPM method uses photometric redshifts of galaxies to search for overdensities around each target along

---

[7] This is equivalent to radii of about 0′.4 at 2.5 < z < 3.5, and 0′.5–0′.6 at 1.35 < z < 2. This radius is more than an order of magnitude smaller than the *Planck* beam (FWHM = 4′.7, and similar to the *Herschel* beam (FWHM ≃ 24″ at 350 μm).

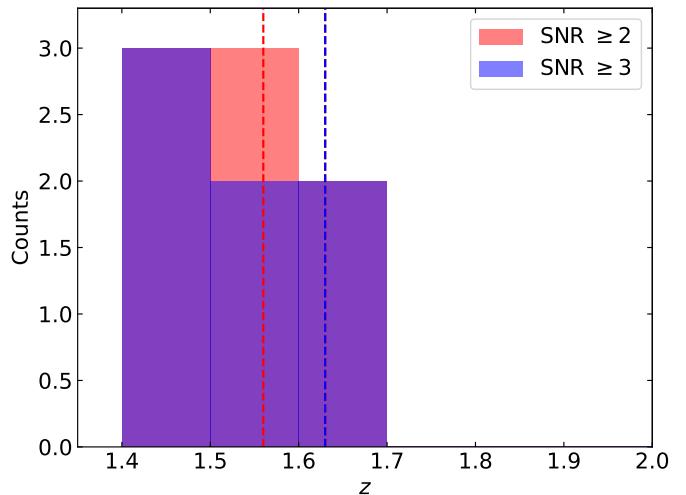**Fig. 2.** Photometric distributions of the *Euclid* overdensities outside *Planck* beams: red, overdensities with S/N ≥ 2; and blue, S/N ≥ 3 outside the *Planck* beams. Vertical dashed lines represent the values corresponding to the detections inside the *Planck* beams, with 2 ≤ S/N < 3 (red dashes) or S/N ≥ 3 (blue dashes).
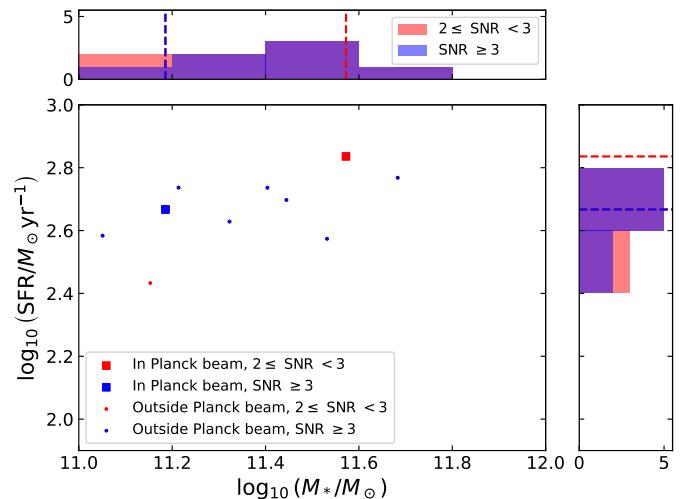

Fig. 3. Star-formation rate as a function of stellar mass of the *Euclid* protocluster candidates. Dots represent overdensities with a signal to noise ratio above 2 or 3 outside the *Planck* beams, depending on their colour. The two squares are the protocluster candidates discussed in this pilot study. Histograms for stellar mass (top) and SFR (right) are plotted using only detections outside the *Planck* beams.

the line of sight. In this work, we used the projected space coordinates of *Planck-Herschel* overdensities, as well as DETECTIFz and DFTE projected space coordinates, separately. To search for associated overdensities, the PPM adopts an accurate sampling of the photometric redshift information to the detriment of a less sophisticated tessellation of the projected space, which is performed in terms of concentric annuli centred around each target. We refer to previous studies for a detailed description of the method (Castignani et al. 2014a,b), its wavelet-based extension (wPPM Castignani et al. 2019), and the applications (Castignani et al. 2014b, 2019; Calvi et al. 2023). To search for PPM overdensities, we used both *Planck* and DETECTIFz protocluster projected coordinates as inputs, separately.

We also use a newly developed detection code for galaxy protoclusters at $z > 1.5$, fine-tuned for a *Euclid*-like wide survey (Ramos Chernenko et al. 2024). The detection code is based on
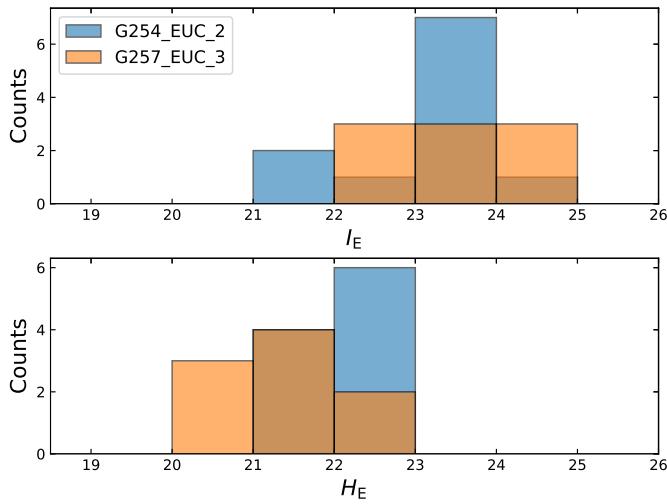
Fig. 4. Histograms of I_E (top panel) and H_E (bottom panel) magnitudes of the galaxies belonging to: G254_EUC_2 (blue); and G257_EUC_3 (orange).

the Monte Carlo Delaunay Tesselation Field Estimator (Schaap & van de Weygaert 2000; Schaap 2007), combined with the Laplacian of Gaussian (Sotak & Boyer 1989; Lindeberg 1992) filter (MC-DTFE-LoG, hereafter), which is conceptually similar to `DETECTIFz`, but enhanced with a multiscale 3D source-detection filter. The 3D Gaussian filters were specifically calibrated using *Euclid*-like protocluster properties from GAEA and MAMBO simulations Euclid Collaboration: Böhringer et al. (2025). The proposed approach is now being tested and validated for a systematic detection of galaxy protoclusters in *Euclid*-like wide surveys using the Q1 data (Chernenko et al. in prep.).

We find that both alternative algorithms detected most structures at the same sky positions and photometric redshifts as those selected by `DETECTIFz`. Table 3 reports the detections and S/N values, similar to those of `DETECTIFz`, which we discuss in Sect. 6.1.

4. *Euclid* counterparts associated with the *Planck* protocluster candidates

4.1. Protoclusters G254_EUC_2 and G257_EUC_3

The two *Euclid* detections that are counterparts of *Planck* protocluster candidates (reported in Table 2) are G254_EUC_2 (S/N = 3.5) with 11 galaxy members at photometric redshift $z_{ph} = 1.63^{+0.19}_{-0.23}$ and G257_EUC_3 (S/N = 2.6) with nine members at $z_{ph} = 1.56^{+0.18}_{-0.21}$. Figure 1 shows the *Euclid* colour images of G254_EUC_2 and G257_EUC_3 and the associated galaxy members.

Figure 4 shows histograms of the I_E and H_E magnitudes of the protocluster members. The fact that we select galaxies with $H_E < 24$ for the protocluster search does not prevent fainter galaxies from belonging to the protocluster (with the same sky positions and photometric redshifts) in principle; however, in this pilot study we hardly encounter such cases. Due to the preselection in photometric redshift and magnitude (see Sect. 3), it is likely that some fainter member galaxies of the overdensities are not detected. Thus, all the parameters, such as the total stellar mass M_* and SFR, should be considered as lower limits.
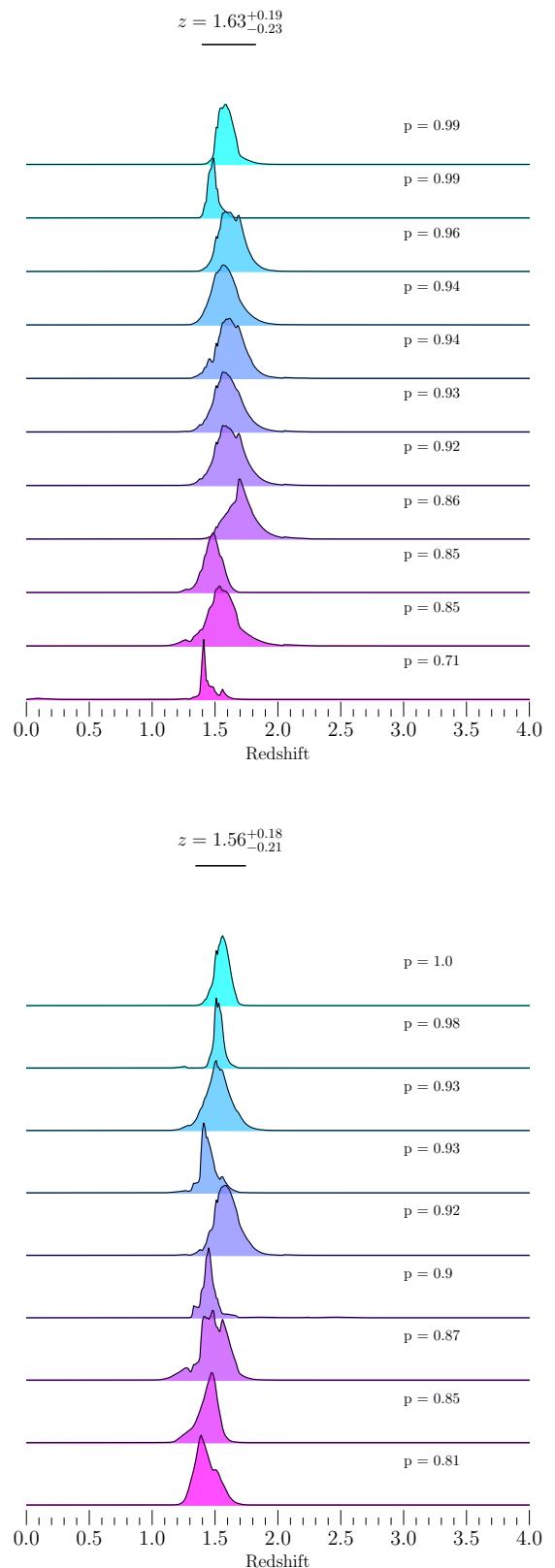

Fig. 5. Photometric redshift distribution functions of each of the sources belonging to the G254_EUC_2 (*top*) and G257_EUC_3 (*bottom*) protocluster candidates, to be confirmed by spectroscopy. The value p is the distribution function integrated over the redshift confidence interval for the protocluster candidate given by `DETECTIFz`, shown at the top of each graph.
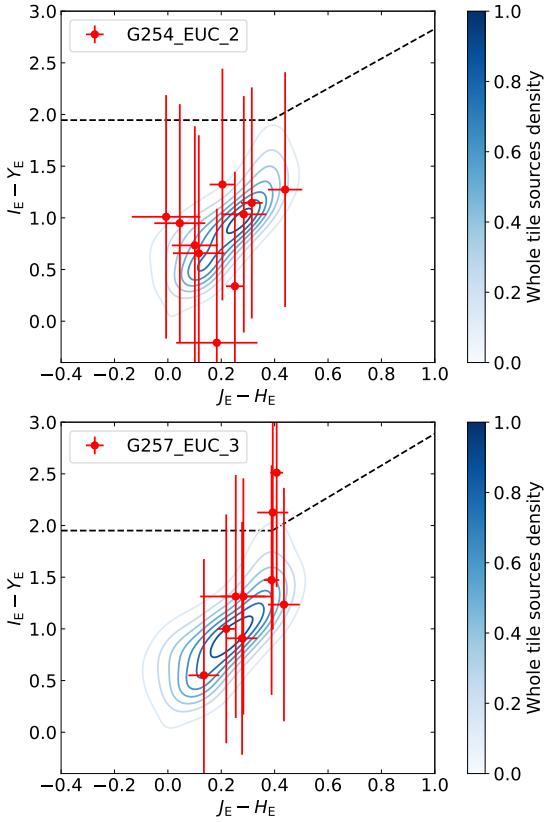
Fig. 6. $I_E - Y_E$ versus $J_E - H_E$ pure *Euclid* colour-colour diagram of galaxies (red circles) belonging to the G254_EUC_2 (*top*) and G257_EUC_3 (*bottom*) protocluster candidates . The colours of all the sources in the tile (more than 100 000) are shown in the blue background density. Three sources of the G257_EUC_3 protocluster candidate are consistent with being powered by an active galactic nucleus. The active galaxies region is delimited by dashed black lines, as defined by Bisigello et al. (2020).

4.2. Euclid protocluster candidates versus Euclid-Planck

To investigate whether the *Euclid-Planck* overdensities are characterised by distinctive properties with respect to the rest of the *Euclid* overdensities, we compare their total SFRs and stellar masses (see Sect. 5.2) in Fig. 3 and distinguish those that fulfill the criterion S/N > 3. The *Euclid-Planck* overdensity subset covers a similar range of SFRs, stellar masses and, richness. We also check the photometric distributions in Fig. 2. It is thus not clear why some of these overdensities are also detected by *Planck* and others are not. We will investigate in the future whether the *Planck* fields host additional overdensities at higher redshifts.

5. Physical characteristics of the *Euclid* counterparts of *Planck* protocluster candidates

5.1. Photometric redshifts and colours

The PDFs of the photometric redshifts of the two protocluster members are shown in Fig. 5. Ensuring a homogeneous distribution of those PDFs is one of the main criteria to retain a protocluster in our final list.

The pure *Euclid* colour-colour diagrams of each protocluster, $I_E - Y_E$ versus $J_E - H_E$, are shown in Fig. 6, following Bisigello et al. (2020). We show the protocluster galaxy members (red points) together with the roughly 100 000 sources in the tile (blue
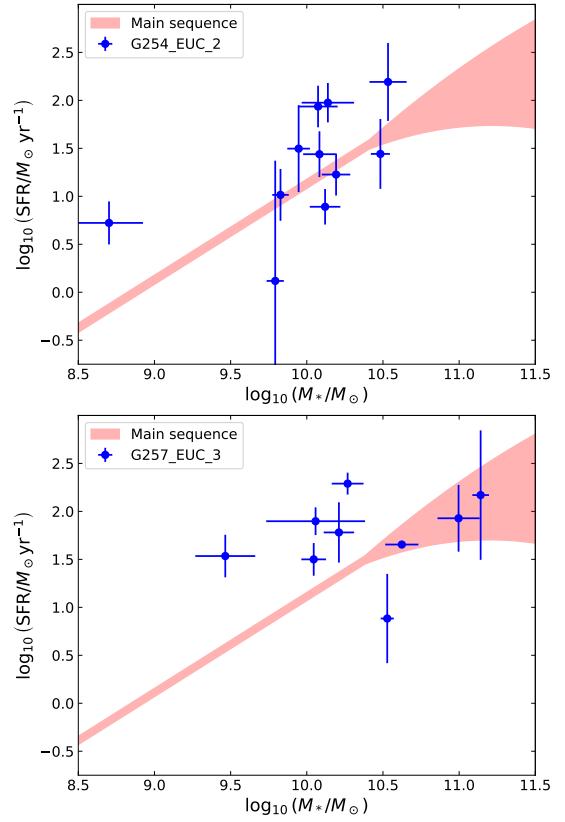
Fig. 7. Star-formation rate (SFR) versus stellar mass (M_*) of member galaxies of the G254_EUC_2 (*top*) and G257_EUC_3 (*bottom*) protocluster candidates. The model of Schreiber et al. (2015) for main sequence galaxies is overplotted as a red area, with model errors derived from the parameters for redshifts $z = 1.63 \pm 0.23$ and $z = 1.56 \pm 0.21$, respectively.

background density). The vast majority of sources are consistent with being star-forming galaxies.

5.2. Physical parameters: stellar masses and star-formation rates

We use the physical parameters derived by the photometric redshift estimation procedure (Euclid Collaboration: Tucci et al. 2025). Figure 7 shows the SFR–M_* relation for the galaxy members of our two protocluster candidates, together with the galaxy-main-sequence model of Schreiber et al. (2015). This relation assumes that SFR and stellar mass M_* are linearly correlated (SFR $\propto M_*$) below a threshold in mass and redshift, above which the SFR decreases, with galaxies gradually quenched.

We observe that in both protocluster candidates, most galaxies lie above the main sequence, a clear sign of starburst activity, yielding total SFR, as estimated using *Euclid* and ground-based data, of $\log_{10}(\text{SFR}/M_\odot\,\text{yr}^{-1}) = 2.75$ for G254_EUC_2 and 2.89 for G257_EUC_3 (Table 2).

We compute the total stellar mass of each protocluster candidate (Table 2 and Fig. 8) by summing up the stellar masses of individual galaxies. This can be taken as a lower limit of the protocluster stellar mass. Indeed, our protocluster members are chosen to have at least 68% probability to be a member, which may be considered too conservative and thus leave the possibility of including more members in a future analysis. In Fig. 8 we report our two protocluster stellar masses versus redshift, together with other protoclusters from the literature (using photometric

or spectroscopic redshifts, see caption). To guide the eye a fit is performed, and our two protoclusters are compatible with values from the literature.

Finally, we report in Table 2 the observed radii of the protoclusters. The values, of the order of 2′, are about a factor of 2 smaller than the predictions of Euclid Collaboration: Böhringer et al. (2025) for protoclusters of mass larger that $10^{14}\,M_\odot$ at $z = 1.5$ or 2.

5.3. Halo masses

To weigh a galaxy protocluster, one might ideally propose to measure the mass using the velocity dispersion of galaxies. Since we would need to detect small differences in velocity, a high precision on redshift measurements would be required, which can only be achieved using spectroscopy. Moreover, this method is based upon the virial theorem, so it requires making the hypothesis that the whole protocluster is virialised, which is of course one of the most important aspects that we want to determine. Another possibility to estimate the halo mass is to detect arcs that are gravitationally lensed by a protocluster. However, such searches are challenging, owing to the rapidly declining sky density of bright background sources for $z > 2$ (Madau & Dickinson 2014). Finally, we could make a compromise and assume that only the core has already undergone virialisation; this hypothesis makes sense, since the infall of matter from the cosmic web should cause intense mixing at the very centre of the gravitational well. There are also methods to estimate the halo mass M_h of each protocluster (Long et al. 2020; Champagne et al. 2021; Daddi et al. 2022; Laporte et al. 2022; Sillassen et al. 2024), scaling from the measurements of the stellar masses of their member galaxies (Behroozi et al. 2013; van der Burg et al. 2014; Behroozi et al. 2019; Legrand et al. 2019; Girelli et al. 2020; Shuntov et al. 2022; Paquereau et al. 2025). In addition to these methods, we also perform an estimation of the dark matter mass of the halo using the universal cosmological baryonic fraction $\Omega_m/\Omega_b - 1 = 5.35$ (Planck Collaboration 2020a,b); we call this 'Method A'.

Halo mass estimates made by scaling to stellar mass is 'Method B'. Uncertainties are computed by propagating the errors on stellar mass from the *Euclid* PHZ PF physical parameter catalogues (Euclid Collaboration: Tucci et al. 2025) and also using each model parameter uncertainty, as provided by Behroozi et al. (2013)[B13], Legrand et al. (2019)[L19], and Shuntov et al. (2022)[S22]. The estimated halo masses are reported in Table 4 for both methods and they are shown in Fig. 9 for Method B [S22]. The three estimates using Method B are consistent within at most 0.5 dex differences, and the halo masses derived using the prescriptions from Legrand et al. (2019) and Shuntov et al. (2022) usually agree to better than 0.1 dex.

6. Discussion

6.1. Line-of-sight effects?

PPM and MC-DTFE-LoG methods find similar sources as `DETECTIFz` (Table 3) and are in agreement with each other. At the location of some of our selected overdensities, other overdensities are detected at higher photometric redshifts. The PPM algorithm also finds, at the location of the *Euclid* `DETECTIFz` source G254_EUC_2 three background overdensities with a S/N of 2.2 each, at redshifts $z = 1.9$, 2.3, and 2.8. For the source G257_EUC_3 background sources are found at redshifts $z = 2.8$ and 3.9 with a S/N of 2.9 each.
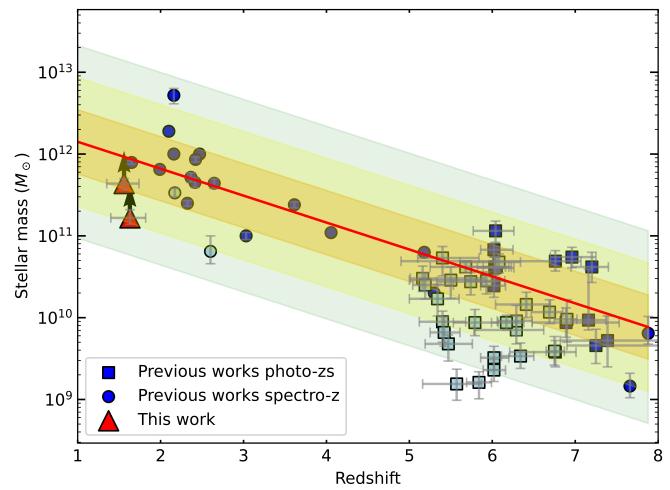

Fig. 8. Stellar mass (lower limits) as a function of redshift for the *Euclid* protoclusters (triangles) and from the literature (circles and squares; Casey 2016; Polletta et al. 2021; Laporte et al. 2022; Morishita et al. 2023, 2024; Sillassen et al. 2024; Gómez-Guijarro et al. 2019; Li et al. 2024; Shimakawa et al. 2024). A fit is performed on the data excluding *Euclid* (red line), with the scatter showed at the $\pm 1\,\sigma$ (orange zone), $\pm 2\,\sigma$ (green zone), and $\pm 3\,\sigma$ (blue zone) levels. Dark blue squares have spectroscopic redshifts and halo masses (and are also plotted in Fig. 9). Light blue squares have spectroscopic redshift but are not shown in Fig. 9.

These multiple detections of background overdensities found with PPM lie at higher redshifts than *Euclid* protocluster candidates, which fit better with Cosmic Noon ($z > 2$). This therefore raises the question of the reliability of matching *Euclid* overdensities with *Planck* protocluster candidates. It is possible that our procedure preferentially detects foreground overdensities, due to photometric redshifts introducing line-of-sight effects. In any case, this issue will be investigated in future using the DR1 data and spectroscopic observations.

6.2. Are they protoclusters? Are they Planck protoclusters?

The two *Euclid* protoclusters (Fig. 9) show characteristics comparable to protoclusters from the literature. Many galaxies in the *Euclid* protoclusters are experiencing a 'star-formation event', or a starburst. This could be another indication that *Euclid* actually detects the counterparts of the *Planck* protocluster candidates. However, there is little direct evidence that these structures are starbursting, despite the high overall SFRs implied by *Planck* (Table 2). Previous studies of the *Planck* protocluster candidates (Polletta et al. 2021, 2022; Kneissl et al. 2019; Hill et al. 2024)) have shown that the majority of the protocluster members are on the star-forming main sequence. This seems to be the case also in other protoclusters like the Spiderweb (Pérez-Martínez et al. 2024a), although not in all, e.g., USS 1558−003 (Pérez-Martínez et al. 2024b) and perhaps our two examples.

Herschel-SPIRE imaging exists in two of the EDFs. Data are described in Oliver et al. (2012) in the EDF-F, and in Planck Collaboration (2015b) in the EDF-S (Table 1). One of our two candidates (G254_EUC_2) also has partial *Herschel* coverage, since it lies close to the edge of the *Herschel* image. For this protocluster candidate we computed the total SFR considering only the *Herschel* sources within the overdensity radius (see Table 2),

Table 2. *Euclid* protoclusters detected with `DETECTIFz` at the location of *Planck+Herschel* protocluster candidates.

Planck + Euclid overdensity name	RA [deg]	Dec [deg]	z_{ph}	N_{gal}	S/N	Overdensity $\log_{10}(1+\delta)$	Radius [arcmin]	Total M_* [$\log_{10}(M_\odot)$]	SFR [$\log_{10}(M_\odot\,yr^{-1})$] *Euclid*	*Planck*	*Herschel*
G254_EUC_2	60.6966	−47.2850	$1.63^{+0.19}_{-0.23}$	11	3.5	0.39	3.05	$11.22^{+0.10}_{-0.08}$	$2.75^{+0.25}_{-0.23}$	$4.03^{+0.15}_{-0.15}$	$4.15^{+0.20}_{-0.20}$
G257_EUC_3	64.0288	−49.4057	$1.56^{+0.18}_{-0.21}$	9	2.6	0.42	1.86	$11.64^{+0.08}_{-0.06}$	$2.89^{+0.27}_{-0.20}$	$4.15^{+0.20}_{-0.20}$	$\cdots$

Notes. Column description: *Planck + Euclid* overdensity name; RA and Dec in degrees; `DETECTIFz` photometric redshift, based on *Euclid* photometric redshifts; number of galaxies in the protocluster; signal-to-noise ratio of the overdensity detection by `DETECTIFz`; `DETECTIFz` overdensity; radius of the protocluster, as estimated by `DETECTIFz` in arcminutes; stellar mass of the protocluster (the sum of stellar masses of all galaxies, coming from *Euclid* PHZ); SFR of the protocluster (the sum of the SFRs of all galaxies, coming from *Euclid* PHZ) in $\log_{10}(M_\odot)$; and the SFR in $\log_{10}(M_\odot\,yr^{-1})$ derived with data from: *Euclid* (lower limits), *Planck*, and *Herschel*. Absence of data is denoted with ellipsis.

Table 3. PPM and MC-DTFE-LoG independent method detections at the locations of the *Euclid* counterparts of the *Planck* protocluster candidates.

Planck name	z_{ph} [PPM]	S/N [PPM]	z_{ph} [MC-DTFE-LoG]	S/N [MC-DTFE-LoG]
G257_EUC_3	1.41 ± 0.09^a	7.7	1.52 ± 0.24	3.4
G254_EUC_2	1.55 ± 0.09^b	3.9	$\cdots$	$\cdots$
G254_EUC_2	1.82 ± 0.09^a	2.4	2.00 ± 0.28	3.2

Notes. To search for PPM overdensities, we used both *Planck* and `DETECTIFz` protocluster projected coordinates as inputs, separately. The corresponding PPM overdensities are denoted with the labels ^{a} and ^{b}, respectively. Columns: field name; PPM redshift of the overdensity (based on photometric redshifts); PPM S/N of detection; MC-DTFE-LoG redshift of the overdensity (based on photometric redshifts); and MC-DTFE-LoG S/N of detection.

Table 4. Halo masses M_h for selected *Euclid* protoclusters detected with `DETECTIFz` at the locations of *Planck+Herschel* protocluster candidates, obtained from the stellar masses with Methods A and B (Sect. 5.3).

Planck + Euclid overdensity name	M_{*c} [$\log_{10}(M_\odot)$]	M_h (A) [$\log_{10}(M_\odot)$)]	M_h (B [B13]) [$\log_{10}(M_\odot)$]	M_h (B [L19]) [$\log_{10}(M_\odot)$]	M_h (B [S22]) [$\log_{10}(M_\odot)$]
G254_EUC_2	$11.22^{+0.10}_{-0.08}$	$11.95^{+0.10}_{-0.08}$	$12.85^{+0.20}_{-0.17}$	$13.01^{+0.17}_{-0.12}$	$12.99^{+0.10}_{-0.07}$
G257_EUC_3	$11.64^{+0.06}_{-0.08}$	$12.37^{+0.06}_{-0.08}$	$13.25^{+0.30}_{-0.24}$	$13.41^{+0.22}_{-0.20}$	$13.38^{+0.17}_{-0.14}$

Notes. Method A uses the Ω_B versus Ω_m ratio and is expected to give lower values (column M_h (A)). Method B uses the stellar to halo mass relations from Behroozi et al. (2013) in column M_h (B [B13]), Legrand et al. (2019) in column M_h (B [L19]) and Shuntov et al. (2022) in column M_h (B [S22]). The first one is applied to the most massive galaxy stellar mass of the protocluster (column M_{*c}) whereas the second and third ones take dark matter haloes of each member galaxy into account. As there could be more galaxy members than the ones we detected, these estimations can be seen as lower limits. The overdensity name refers to the Table 2. We plot in Fig. 9 M_h (B [S22]) versus redshift. Uncertainties come from both the measured stellar masses and the models linking stellar masses to halo masses (see sect. 5.3).

and with $> 3\,\sigma$ detections in all three SPIRE bands. We fitted the submm data of each selected *Herschel* source with a modified blackbody using the `cmcirsed` package (Casey 2012), with a dust-emissivity index $\beta = 1.8$ (Cortese et al. 2014; Pokhrel et al. 2016), and assuming the protocluster redshift. To avoid contamination from *Herschel* sources at a redshift incompatible with that of the protocluster candidate, we included in the total SFR estimate only the sources for which the fit yields a dust temperature between 15 K and 50 K. The SFR of each source was derived from the total FIR luminosity as SFR $= 1.48\times10^{-10}\,L(\text{FIR})$ (Kennicutt & Evans 2012). In Table 2, we report the total SFR. We select one *Herschel* source for G254_EUC_2 ; the *Herschel*-based total SFR is 1.5–40 times larger than the values derived from the *Euclid* PHZ. This wide disparity might be explained by incompleteness in the *Euclid*-selected members, as well as by contamination of *Herschel* sources that are not protocluster members. A search for counterparts of these *Euclid* protoclusters in the eROSITA (Merloni et al. 2024) and the South Pole Telescope (SPT, Bocquet et al. 2019) cluster catalogues shows no association.

6.3. Their evolutionary state: are they in the 'dying protocluster' phase?

The two protoclusters discussed in this pilot study show fairly high SFRs (about 500–800 $M_\odot\,yr^{-1}$), and are located in redshift towards the end of Cosmic Noon, at $z_{ph} \simeq 1.6$. In this redshift range, several mature galaxy clusters have already been detected (e.g., Willis et al. 2020; Stanford et al. 2012; Gobat et al. 2013; Andreon et al. 2014; Strazzullo et al. 2023). The star-forming nature of the member galaxies and the high total SFRs suggest that these protoclusters might be in an earlier evolutionary stage, rather than being like the more mature coeval galaxy clusters. However, this star-formation activity is not expected to be fuelled by cold gas accretion, since the gas is presumed to be shock heated, as illustrated in Fig. 9. Thus, we are led to ask what makes these protoclusters special at these relatively low redshifts? Will some of these structures *not* become galaxy clusters? In which evolutionary state are we observing these protoclusters? And how is the observed star-formation activity sustained? While it is difficult to accurately answer these questions, given the available data, we may provide a hypothesis.
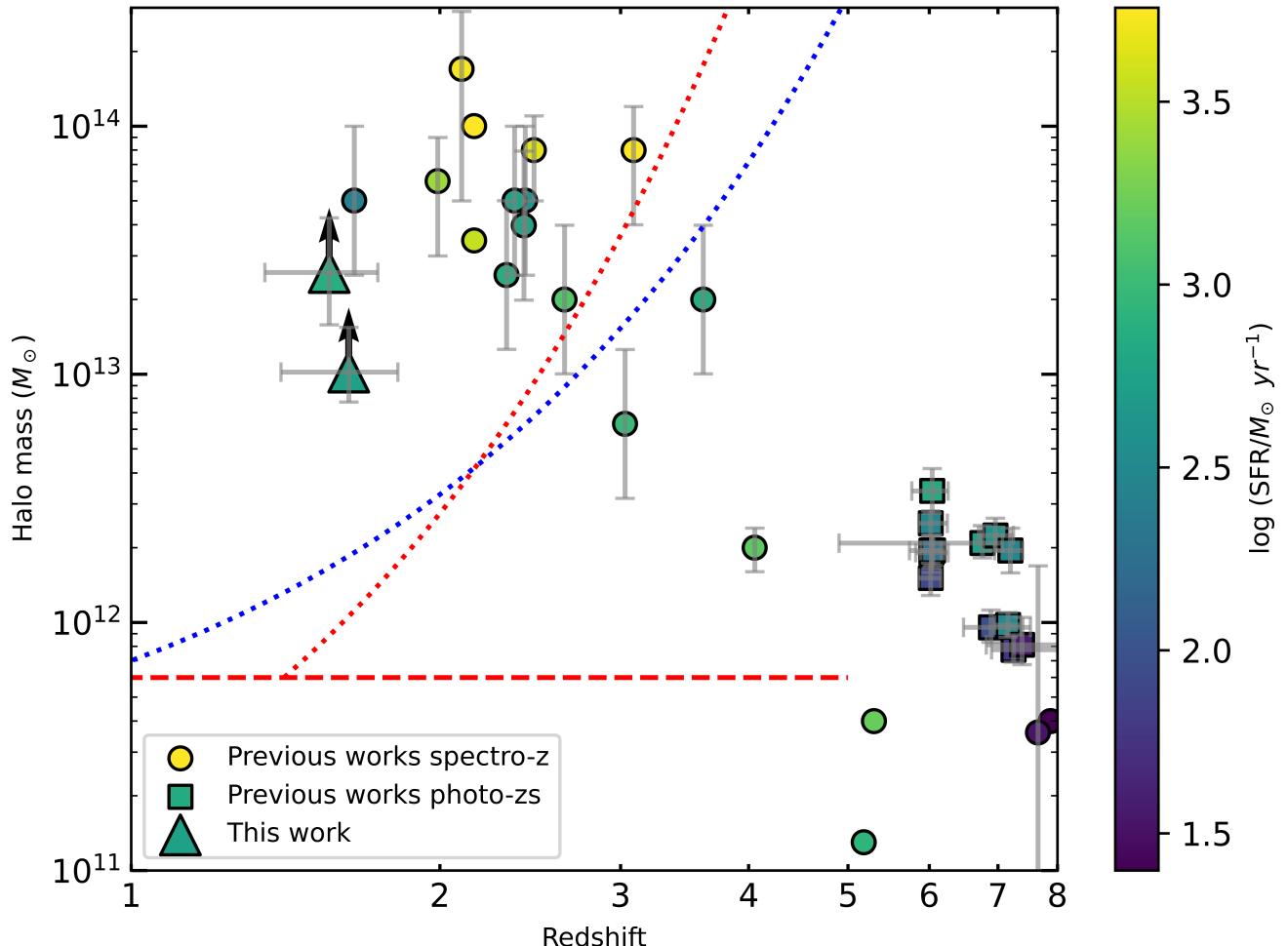
Fig. 9. Protocluster halo mass (M_h) versus redshift z (notice the log-log scale), colour-coded by star-formation rate (SFR, colour bar). *Euclid* protocluster lower limits: triangles, using Method B [S22] (Shuntov et al. (2022), see Sect. 5.3 for details. Circles are protoclusters from the literature: Casey (2016); Polletta et al. (2021); Laporte et al. (2022); Morishita et al. (2023); Morishita et al. (2024); Sillassen et al. (2024); and Shimakawa et al. (2024). The lines illustrate the different predicted gas-cooling regimes: dotted lines come from Dekel & Birnboim (2006) (red dashes) and Daddi et al. (2022) (blue dashes) and separate loci of cold gas in a hot medium (top right) and hot gas (top left); halo masses below the horizontal red dashed line M_{shock}, coming from Dekel & Birnboim (2006), are predicted to contain only cold flows with no shock heating within haloes at $z < 5$.

Using molecular gas observations, Polletta et al. (2022) (their section 4.9) found that other *Planck* protoclusters located at $z > 2$ exhibit gas depletion times of the order of 0.47 ± 0.07 Gyr, and are thus expected to exhaust their cold gas at around $z = 1.1$–1.6. Might we actually be observing these 'dying protoclusters', and looking at the 'protocluster swan song', i.e., their last unsustainable star-formation event (or star-formation event before a complete exhaustion of gas for star formation)? The end of this dying protocluster phase may mark the actual 'birth' of a galaxy cluster. Molecular gas observations will be needed to answer this question.

7. Prospects for future detections of galaxy protoclusters in *Euclid* surveys

Looking ahead, beyond the first detections of protoclusters in Q1 study, we can ask ourselves what will be the properties (especially the redshift distribution) of the protoclusters that will be detected by *Euclid* in the future. Simulations described in Euclid Collaboration: Böhringer et al. (2025) provide forecasts on abundance, and sky-filling as a function of redshift, among other observables. They show that *Euclid* should detect a protocluster density of around 8 deg^2 at $z = 1.5$–2, with masses greater than $10^{14}\,M_\odot$.

Another empirical way to predict the detectability of galaxy protoclusters in the EWS and Euclid Deep Survey (EDS) is to scale from existing protoclusters. We use here individual galaxies belonging to spectroscopically confirmed protoclusters
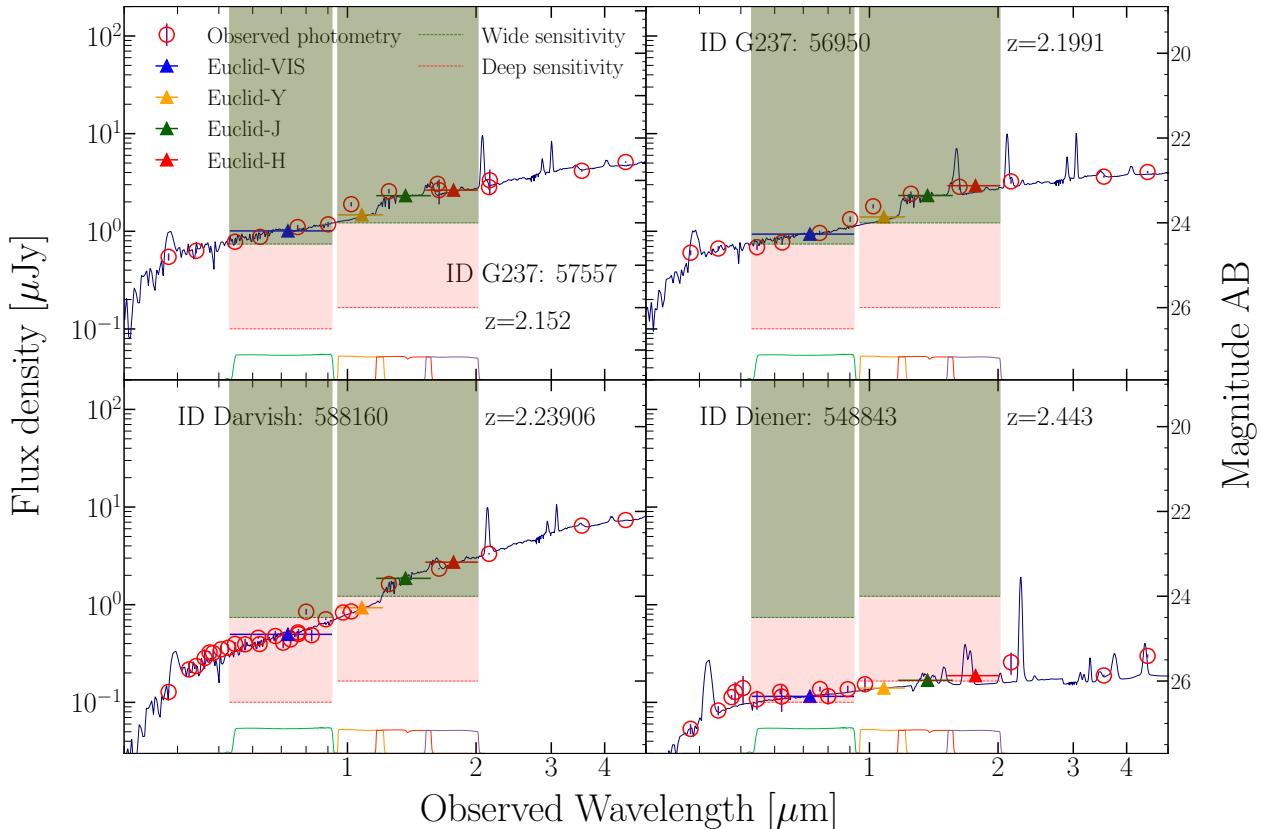
Fig. 10. Four galaxy SEDs of spectroscopically confirmed protoclusters from Polletta et al. (2021), Diener et al. (2015), and Darvish et al. (2020), and their fits using `Prospector` (Johnson et al. 2021). Circles are photometric points, while coloured triangles are interpolated flux densities in the *Euclid* photometric bands. The green zone shows the detection limits for the Euclid Wide Survey and the red zone shows the detection limits for the Euclid Deep Survey. The *Euclid* bandpasses are represented in the bottom of each panel. The detectability zones (green for EWS, red for EDS) illustrate the areas where galaxies will be detected by *Euclid*.

around $z = 2$ from Diener et al. (2015), Wang et al. (2016), Darvish et al. (2020), and Polletta et al. (2021), and thus not from the two *Euclid* protoclusters discussed above. This redshift range is similar to the photometric redshifts of our detections. We fit the SEDs of the individual galaxies using `Prospector` (Johnson et al. 2021) on Fig. 10. By redshifting the SED fits and convolving them with the *Euclid* photometric filters (Fig. 11), we can predict the flux densities of these protocluster galaxies in the VIS and NIR bands as a function of redshift.

We use this method with 79 galaxies from the literature with redshifts confirmed spectroscopically. We define a criterion of detecting at least 50% of those galaxies at a given redshift and in at least one *Euclid* band (usually H_E) to qualify a protocluster detected. We empirically find that the EWS should allow us to detect protoclusters out to $z = 3$, and the EDS out to $z = 5.5$. This approach, however, does not assess the purity or completeness of samples, but only gives a useful first-order prediction. The protoclusters that we find here in the Q1 data set at the EWS depth are currently compatible in terms of redshift range with these empirical predictions, as well as with the predictions in Euclid Collaboration: Böhringer et al. (2025).

Finally, high redshift ($z > 1.3$) *Spitzer* counterparts were recently found in EDFs (Euclid Collaboration: Mai et al. 2025). It has been shown that these counterparts consist of a majority of passive galaxies, which we expect to find in protoclusters at the last stage of the Cosmic Noon. According to (Euclid Collaboration: Mai et al. 2025), these overdense regions could host galaxy clusters and/or protoclusters. We therefore expect *Euclid*

to detect many more new protoclusters, which will help us better understand them.

With the experience gained in this Q1 study, we anticipate that using at least two algorithms in sequence, like `DETECTIFz` or MC-DTFE-LoG, and then PPM, will increase the reliability of the protocluster search. Indeed, comparing each detection along the line of sight, especially the S/N and the photometric redshift of the overdensities, may be crucial to unveil fainter structures.

8. Conclusions

We have searched in the *Euclid* Q1 data for galaxy protoclusters counterparts of *Planck* protocluster candidates. In 11 tiles, we found 10 protoclusters candidates, and focused on the two of them coincident with *Planck* PHz candidates. For these structures we estimated the photometric redshifts, as well as lower limits for stellar mass, star-formation rate, and halo mass estimates. We detected most of the overdensities with two independent algorithms, providing converging estimates on the significance and mean photometric redshifts.

Our detections are situated at redshifts $1.5 < z < 2.0$, slightly below the expected *Planck* selection and previous follow-up observations of *Planck* candidate protoclusters. However, it is worth noting that the protocluster-finder algorithm used in this study also finds some galaxy overdensities at lower S/N and higher redshift. At this stage, it is difficult to rule out the possibility that our current procedure primarily selects foreground line-of-sight overdensities more efficiently in the *Euclid* data than at
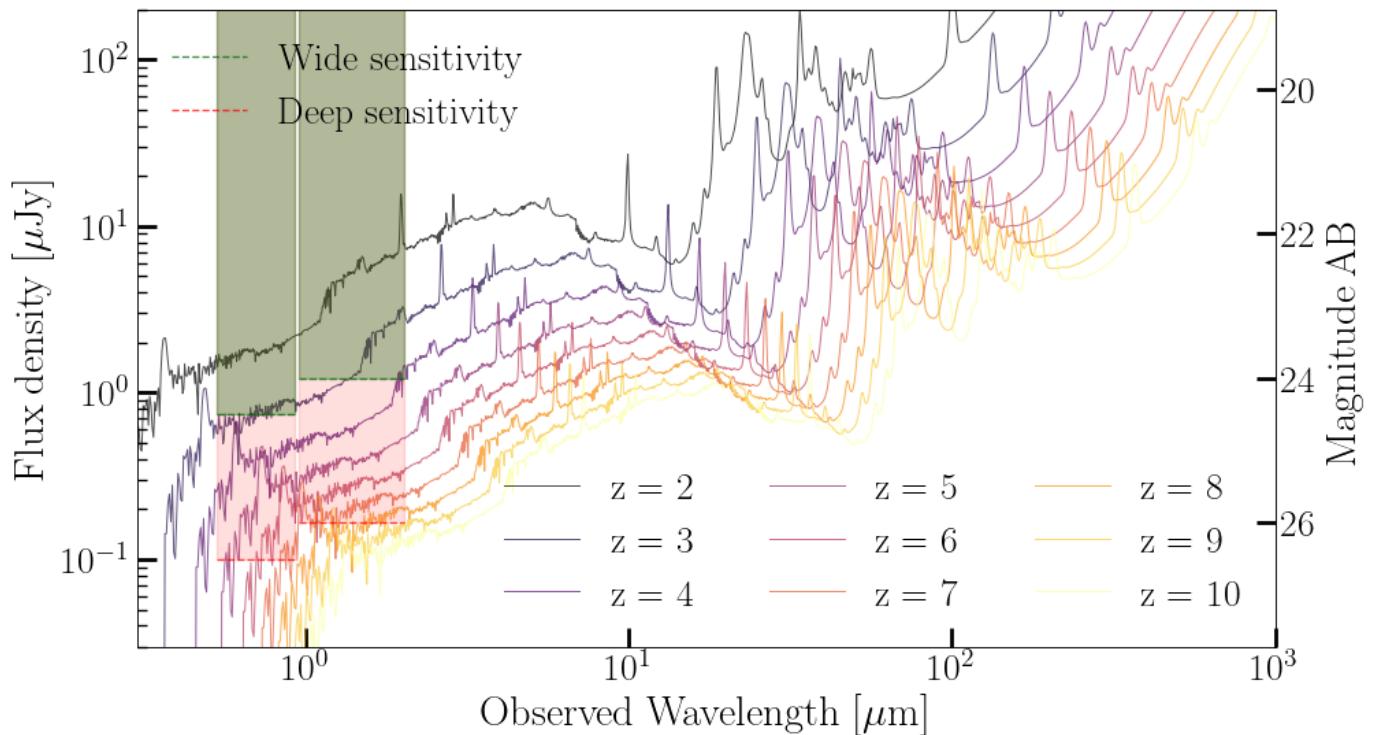
Fig. 11. SED of the $z = 2.1576$ galaxy 55326 in G237 from Polletta et al. (2021), redshifted up to $z = 10$. The flux densities in the observed *Euclid* bands SED are obtained at each redshift. The comparison with the survey sensitivities (same colours as Fig. 10) allows an estimate of the limiting redshift for detection.

higher redshift ($z > 2$). However, we favour a conservative approach and focus on the high reliability detections rather than choosing higher-redshift (but lower S/N) counterparts as the actual *Planck* protocluster candidates counterparts.

The *Euclid* counterparts of the *Planck* candidates occupy an interesting location in the halo-mass–redshift plane, $13.0 < \log_{10} M_{\rm h} < 13.5$ and $1.5 < z < 2$, close to the expected transition between cold flows with no shock heating throughout the halo to shock heating in the halo. A first search for counterparts of these *Euclid* protoclusters in the eROSITA and SPT cluster catalogues shows no association; this suggests that the halos do not contain gas that is hot enough to emit in the X-ray or to cast shadows in the cosmic microwave background via the Sunyaev-Zeldovich effect.

The estimated lower limits of $M_{\rm h}$, together with the photometric redshift range (towards the end of Cosmic Noon) probed, and the star-formation rates of the protoclusters, raise several unanswered questions. Are these four protoclusters representative of the *Planck* protocluster candidate sample? Previous observations tended to detect higher redshift and higher SFR protoclusters, sometimes with a few structures along the line of sight. Is this pilot programme missing fainter galaxies in the overdensities, or higher redshift overdensities? Are we witnessing the dying phase of protoclusters (or the protocluster 'swan song')? Indeed we may expect the measured star-formation activity to be unsustainable, and thus we may be witnessing the last major star-forming event. What is the maturity level of the detected protoclusters? Do they contain gas and what state is it in?

Additional data, such as from *Spitzer* (e.g., Martinache et al. 2018; Euclid Collaboration: Mai et al. 2025), where available, will be helpful to better constrain the galaxy SEDs and photometric redshifts. Future observations and analyses in the millimetre with SPT, in the X-rays with eROSITA or the 'XMM

Fornax heritage programme'[8], and optical/NIR/mm/radio spectroscopy (including *Euclid* spectra in the near-infrared) will help to obtain a clearer view of these structures and on the thousands of protoclusters that will be detected in the forthcoming *Euclid* DR1 data set. Indeed, in total, we can expect of the order of 40 000 protoclusters with a mass limit of $M \geq 8 \times 10^{13} M_{\odot}$ in the complete EWS in the redshift range $z = 1.5$–4 (Euclid Collaboration: Böhringer et al. 2025).

References

Aihara, H., Arimoto, N., Armstrong, R., et al. 2018, PASJ, 70, S4

Alberts, S. & Noble, A. 2022, Universe, 8, 554

Albrecht, A., Bernstein, G., Cahn, R., et al. 2006, arXiv e-prints, arXiv:0609591

Andreon, S., Newman, A. B., Trinchieri, G., et al. 2014, A&A, 565, A120

Behroozi, P., Wechsler, R. H., Hearin, A. P., & Conroy, C. 2019, MNRAS, 488, 3143

Behroozi, P. S., Wechsler, R. H., & Conroy, C. 2013, ApJ, 770, 57

Bisigello, L., Kuchner, U., Conselice, C. J., et al. 2020, MNRAS, 494, 2337

Bocquet, S., Dietrich, J. P., Schrabback, T., et al. 2019, ApJ, 878, 55

Calvi, R., Castignani, G., & Dannerbauer, H. 2023, A&A, 678, A15

Calvi, R., Dannerbauer, H., Arrabal Haro, P., et al. 2021, MNRAS, 502, 4558

Casey, C. M. 2012, MNRAS, 425, 3094

Casey, C. M. 2016, ApJ, 824, 36

Casey, C. M., Cooray, A., Capak, P., et al. 2015, ApJ, 808, L33

Castignani, G., Chiaberge, M., Celotti, A., & Norman, C. 2014a, ApJ, 792, 113

Castignani, G., Chiaberge, M., Celotti, A., Norman, C., & De Zotti, G. 2014b, ApJ, 792, 114

Castignani, G., Combes, F., Salomé, P., et al. 2019, A&A, 623, A48

Champagne, J. B., Casey, C. M., Zavala, J. A., et al. 2021, ApJ, 913, 110

Chapman, S. C., Blain, A., Ibata, R., et al. 2009, ApJ, 691, 560

Chiang, Y.-K., Overzier, R., & Gebhardt, K. 2013, ApJ, 779, 127

Chiang, Y.-K., Overzier, R. A., Gebhardt, K., & Henriques, B. 2017, ApJ, 844, L23

Clements, D. L., Braglia, F. G., Hyde, A. K., et al. 2014, MNRAS, 439, 1193

Coogan, R. T., Daddi, E., Sargent, M. T., et al. 2018, MNRAS, 479, 703

Cortese, L., Fritz, J., Bianchi, S., et al. 2014, MNRAS, 440, 942

Daddi, E., Delvecchio, I., Dimauro, P., et al. 2022, A&A, 661, L7

Darvish, B., Scoville, N. Z., Martin, C., et al. 2020, ApJ, 892, 8

Dekel, A. & Birnboim, Y. 2006, MNRAS, 368, 2

Diener, C., Lilly, S. J., Ledoux, C., et al. 2015, ApJ, 802, 31

Emonts, B. H. C., Cai, Z., Prochaska, J. X., Li, Q., & Lehnert, M. D. 2019, ApJ, 887, 86

Euclid Collaboration: Aussel, H., Tereno, I., Schirmer, M., et al. 2025, A&A, submitted, arXiv:2503.15302

Euclid Collaboration: Böhringer, H., Chon, G., Cucciati, O., et al. 2025, A&A, 693, A59

Euclid Collaboration: Cropper, M., Al Bahlawan, A., Amiaux, J., et al. 2024, A&A, accepted, arXiv:2405.13492

Euclid Collaboration: Jahnke, K., Gillard, W., Schirmer, M., et al. 2024, A&A, accepted, arXiv:2405.13493

Euclid Collaboration: Mai, N., Mei, S., Cleland, C., et al. 2025, A&A, submitted, arXiv:2503.15331

Euclid Collaboration: McCracken, H. J., Benson, K., Dolding, C., et al. 2025, A&A, submitted, arXiv:2503.15303

Euclid Collaboration: Mellier, Y., Abdurro'uf, Acevedo Barroso, J., et al. 2024, A&A, accepted, arXiv:2405.13491

Euclid Collaboration: Polenta, G., Frailis, M., Alavi, A., et al. 2025, A&A, submitted, arXiv:2503.15304

Euclid Collaboration: Romelli, E., Kümmel, M., Dole, H., et al. 2025, A&A, submitted, arXiv:2503.15305

Euclid Collaboration: Tucci, M., Paltani, S., Hartley, W. G., et al. 2025, A&A, submitted, arXiv:2503.15306

Euclid Quick Release Q1. 2025, `https://doi.org/10.57780/esa-2853f3b`

Flores-Cacho, I., Pierini, D., Soucail, G., et al. 2016, A&A, 585, A54

Girelli, G., Pozzetti, L., Bolzonella, M., et al. 2020, A&A, 634, A135

Gobat, R., Strazzullo, V., Daddi, E., et al. 2013, ApJ, 776, 9

Gómez-Guijarro, C., Riechers, D. A., Pavesi, R., et al. 2019, ApJ, 872, 117

Gómez-Guijarro, C., Toft, S., Karim, A., et al. 2018, ApJ, 856, 121

Gouin, C., Aghanim, N., Dole, H., Polletta, M., & Park, C. 2022, A&A, 664, A155

Griffin, M. J., Abergel, A., Abreu, A., et al. 2010, A&A, 518, L3

Hill, R., Polletta, M. d. C., Bethermin, M., et al. 2024, arXiv e-prints, arXiv:2412.00294

Johnson, B. D., Leja, J., Conroy, C., & Speagle, J. S. 2021, ApJS, 254, 22

Kennicutt, R. C. & Evans, N. J. 2012, ARA&A, 50, 531

Kneissl, R., Polletta, M. d. C., Martinache, C., et al. 2019, A&A, 625, A96

Koyama, Y., Kodama, T., Tadaki, K.-i., et al. 2013, MNRAS, 428, 1551

Koyama, Y., Polletta, M. d. C., Tanaka, I., et al. 2021, MNRAS, 503, L1

Kubo, M., Yamada, T., Ichikawa, T., et al. 2015, ApJ, 799, 38

Laporte, N., Zitrin, A., Dole, H., et al. 2022, A&A, 667, L3

Legrand, L., McCracken, H. J., Davidzon, I., et al. 2019, MNRAS, 486, 5468

Li, Q., Conselice, C. J., Sarron, F., et al. 2024, arXiv e-prints, arXiv:2405.17359

Lindeberg, T. 1992, Journal of Mathematical Imaging and Vision, 1, 65

Long, A. S., Cooray, A., Ma, J., et al. 2020, ApJ, 898, 133

Madau, P. & Dickinson, M. 2014, ARA&A, 52, 415

Martig, M., Bournaud, F., Teyssier, R., & Dekel, A. 2009, ApJ, 707, 250

Martinache, C., Rettura, A., Dole, H., et al. 2018, A&A, 620, A198

Merloni, A., Lamer, G., Liu, T., et al. 2024, A&A, 682, A34

Miller, T. B., Chapman, S. C., Aravena, M., et al. 2018, Nature, 556, 469

Morishita, T., Liu, Z., Stiavelli, M., et al. 2024, arXiv e-prints, arXiv:2408.10980

Morishita, T., Roberts-Borsani, G., Treu, T., et al. 2023, ApJ, 947, L24

Muldrew, S. I., Hatch, N. A., & Cooke, E. A. 2015, MNRAS, 452, 2528

Negrello, M., Gonzalez-Nuevo, J., De Zotti, G., et al. 2017, MNRAS, 470, 2253

Nelson, D., Springel, V., Pillepich, A., et al. 2019, Computational Astrophysics and Cosmology, 6, 2

Oliver, S. J., Bock, J., Altieri, B., et al. 2012, MNRAS, 424, 1614

Oteo, I., Ivison, R. J., Dunne, L., et al. 2018, ApJ, 856, 72

Overzier, R. A. 2016, A&A Rev., 24, 14

Paquereau, L., Laigle, C., McCracken, H. J., et al. 2025, arXiv e-prints, arXiv:2501.11674

Pérez-Martínez, J. M., Dannerbauer, H., Emonts, B. H. C., et al. 2024a, arXiv e-prints, arXiv:2411.12138

Pérez-Martínez, J. M., Kodama, T., Koyama, Y., et al. 2024b, MNRAS, 527, 10221

Pillepich, A., Springel, V., Nelson, D., et al. 2018, MNRAS, 473, 4077

Planck Collaboration. 2015a, A&A, 581, A14

Planck Collaboration. 2015b, A&A, 582, A30

Planck Collaboration. 2016, A&A, 596, A100

Planck Collaboration. 2020a, A&A, 641, A1

Planck Collaboration. 2020b, A&A, 641, A6

Pokhrel, R., Gutermuth, R., Ali, B., et al. 2016, MNRAS, 461, 22

Polletta, M., Dole, H., Martinache, C., et al. 2022, A&A, 662, A85

Polletta, M., Frye, B. L., Garuda, N., et al. 2024, A&A, 690, A285

Polletta, M., Soucail, G., Dole, H., et al. 2021, A&A, 654, A121

Ramos Chernenko, N., Bonjean, V., Dannerbauer, H., Gutiérrez de La Cruz, C., & Cucciati, O. 2024, in EAS2024, European Astronomical Society Annual Meeting, 2014

Remus, R.-S., Dolag, K., & Dannerbauer, H. 2023, ApJ, 950, 191

Rotermund, K. M., Chapman, S. C., Phadke, K. A., et al. 2021, MNRAS, 502, 1797

Sarron, F. & Conselice, C. J. 2021, MNRAS, 506, 2136

Schaap, W. E. 2007, PhD thesis, University of Groningen, Netherlands

Schaap, W. E. & van de Weygaert, R. 2000, A&A, 363, L29

Schawinski, K., Urry, C. M., Simmons, B. D., et al. 2014, MNRAS, 440, 889

Schreiber, C., Pannella, M., Elbaz, D., et al. 2015, A&A, 575, A74

Shi, K., Huang, Y., Lee, K.-S., et al. 2019, ApJ, 879, 9

Shimakawa, R., Pérez-Martínez, J. M., Dannerbauer, H., et al. 2024, ApJ, 977, 73

Shuntov, M., McCracken, H. J., Gavazzi, R., et al. 2022, A&A, 664, A61

Sillassen, N. B., Jin, S., Magdis, G. E., et al. 2024, A&A, 690, A55

Soifer, B. T., Helou, G., & Werner, M. 2008, ARA&A, 46, 201

Sotak, G. & Boyer, K. 1989, Computer Vision, Graphics, and Image Processing, 48, 147

Stanford, S. A., Brodwin, M., Gonzalez, A. H., et al. 2012, ApJ, 753, 164

Steidel, C. C., Adelberger, K. L., Shapley, A. E., et al. 2000, ApJ, 532, 170

Strazzullo, V., Pannella, M., Mohr, J. J., et al. 2023, A&A, 669, A131

Tadaki, K.-i., Kodama, T., Hayashi, M., et al. 2019, PASJ, 71, 40

van der Burg, R. F. J., Muzzin, A., Hoekstra, H., et al. 2014, A&A, 561, A79

Wang, T., Elbaz, D., Daddi, E., et al. 2016, ApJ, 828, 56

Werner, M. W., Roellig, T. L., Low, F. J., et al. 2004, ApJS, 154, 1

Willis, J. P., Canning, R. E. A., Noordeh, E. S., et al. 2020, Nature, 577, 39

[1] Université Paris-Saclay, CNRS, Institut d'astrophysique spatiale, 91405, Orsay, France
[2] Institut de Recherche en Informatique de Toulouse (IRIT), Université de Toulouse, CNRS, Toulouse INP, UT3, 31062 Toulouse, France
[3] Laboratoire MCD, Centre de Biologie Intégrative (CBI), Université de Toulouse, CNRS, UT3, 31062 Toulouse, France
[4] INAF-Osservatorio di Astrofisica e Scienza dello Spazio di Bologna, Via Piero Gobetti 93/3, 40129 Bologna, Italy
[5] Instituto de Astrofísica de Canarias, Vía Láctea, 38205 La Laguna, Tenerife, Spain
[6] Instituto de Astrofísica de Canarias (IAC); Departamento de Astrofísica, Universidad de La Laguna (ULL), 38200, La Laguna, Tenerife, Spain
[7] Université Paris-Saclay, CEA, Département d'Électronique des Détecteurs et d'Informatique pour la Physique, 91191, Gif-sur-Yvette, France
[8] Université Paris-Saclay, CNRS, Inria, LISN, 91191, Gif-sur-Yvette, France
[9] Department of Astronomy/Steward Observatory, University of Arizona, 933 N. Cherry Avenue, Tucson, AZ 85721, USA
[10] INAF-IASF Milano, Via Alfonso Corti 12, 20133 Milano, Italy
[11] Department of Astronomy & Astrophysics, University of California at San Diego, 9500 Gilman Drive, La Jolla, CA 92093, USA
[12] INAF-Osservatorio Astronomico di Trieste, Via G. B. Tiepolo 11, 34143 Trieste, Italy
[13] IFPU, Institute for Fundamental Physics of the Universe, via Beirut 2, 34151 Trieste, Italy
[14] ESAC/ESA, Camino Bajo del Castillo, s/n., Urb. Villafranca del Castillo, 28692 Villanueva de la Cañada, Madrid, Spain
[15] School of Mathematics and Physics, University of Surrey, Guildford, Surrey, GU2 7XH, UK
[16] INAF-Osservatorio Astronomico di Brera, Via Brera 28, 20122 Milano, Italy
[17] INFN, Sezione di Trieste, Via Valerio 2, 34127 Trieste TS, Italy
[18] SISSA, International School for Advanced Studies, Via Bonomea 265, 34136 Trieste TS, Italy
[19] Dipartimento di Fisica e Astronomia, Università di Bologna, Via Gobetti 93/2, 40129 Bologna, Italy
[20] INFN-Sezione di Bologna, Viale Berti Pichat 6/2, 40127 Bologna, Italy
[21] INAF-Osservatorio Astronomico di Padova, Via dell'Osservatorio 5, 35122 Padova, Italy
[22] Space Science Data Center, Italian Space Agency, via del Politecnico snc, 00133 Roma, Italy
[23] INAF-Osservatorio Astrofisico di Torino, Via Osservatorio 20, 10025 Pino Torinese (TO), Italy
[24] Dipartimento di Fisica, Università di Genova, Via Dodecaneso 33, 16146, Genova, Italy
[25] INFN-Sezione di Genova, Via Dodecaneso 33, 16146, Genova, Italy
[26] Department of Physics "E. Pancini", University Federico II, Via Cinthia 6, 80126, Napoli, Italy
[27] INAF-Osservatorio Astronomico di Capodimonte, Via Moiariello 16, 80131 Napoli, Italy
[28] Instituto de Astrofísica e Ciências do Espaço, Universidade do Porto, CAUP, Rua das Estrelas, PT4150-762 Porto, Portugal
[29] Faculdade de Ciências da Universidade do Porto, Rua do Campo de Alegre, 4150-007 Porto, Portugal
[30] Dipartimento di Fisica, Università degli Studi di Torino, Via P. Giuria 1, 10125 Torino, Italy
[31] INFN-Sezione di Torino, Via P. Giuria 1, 10125 Torino, Italy
[32] Centro de Investigaciones Energéticas, Medioambientales y Tecnológicas (CIEMAT), Avenida Complutense 40, 28040 Madrid, Spain
[33] Port d'Informació Científica, Campus UAB, C. Albareda s/n, 08193 Bellaterra (Barcelona), Spain
[34] Institute for Theoretical Particle Physics and Cosmology (TTK), RWTH Aachen University, 52056 Aachen, Germany
[35] INAF-Osservatorio Astronomico di Roma, Via Frascati 33, 00078 Monteporzio Catone, Italy
[36] INFN section of Naples, Via Cinthia 6, 80126, Napoli, Italy
[37] Institute for Astronomy, University of Hawaii, 2680 Woodlawn Drive, Honolulu, HI 96822, USA
[38] Dipartimento di Fisica e Astronomia "Augusto Righi" - Alma Mater Studiorum Università di Bologna, Viale Berti Pichat 6/2, 40127 Bologna, Italy
[39] Institute for Astronomy, University of Edinburgh, Royal Observatory, Blackford Hill, Edinburgh EH9 3HJ, UK
[40] Jodrell Bank Centre for Astrophysics, Department of Physics and Astronomy, University of Manchester, Oxford Road, Manchester M13 9PL, UK
[41] European Space Agency/ESRIN, Largo Galileo Galilei 1, 00044 Frascati, Roma, Italy
[42] Université Claude Bernard Lyon 1, CNRS/IN2P3, IP2I Lyon, UMR 5822, Villeurbanne, F-69100, France
[43] Aix-Marseille Université, CNRS, CNES, LAM, Marseille, France
[44] Institut de Ciències del Cosmos (ICCUB), Universitat de Barcelona (IEEC-UB), Martí i Franquès 1, 08028 Barcelona, Spain
[45] Institució Catalana de Recerca i Estudis Avançats (ICREA), Passeig de Lluís Companys 23, 08010 Barcelona, Spain
[46] UCB Lyon 1, CNRS/IN2P3, IUF, IP2I Lyon, 4 rue Enrico Fermi, 69622 Villeurbanne, France
[47] Mullard Space Science Laboratory, University College London, Holmbury St Mary, Dorking, Surrey RH5 6NT, UK
[48] Departamento de Física, Faculdade de Ciências, Universidade de Lisboa, Edifício C8, Campo Grande, PT1749-016 Lisboa, Portugal
[49] Instituto de Astrofísica e Ciências do Espaço, Faculdade de Ciências, Universidade de Lisboa, Campo Grande, 1749-016 Lisboa, Portugal
[50] Department of Astronomy, University of Geneva, ch. d'Ecogia 16, 1290 Versoix, Switzerland
[51] INAF-Istituto di Astrofisica e Planetologia Spaziali, via del Fosso del Cavaliere, 100, 00100 Roma, Italy
[52] INFN-Padova, Via Marzolo 8, 35131 Padova, Italy
[53] Aix-Marseille Université, CNRS/IN2P3, CPPM, Marseille, France
[54] INFN-Bologna, Via Irnerio 46, 40126 Bologna, Italy
[55] Institut d'Estudis Espacials de Catalunya (IEEC), Edifici RDIT, Campus UPC, 08860 Castelldefels, Barcelona, Spain
[56] Institute of Space Sciences (ICE, CSIC), Campus UAB, Carrer de Can Magrans, s/n, 08193 Barcelona, Spain
[57] School of Physics, HH Wills Physics Laboratory, University of Bristol, Tyndall Avenue, Bristol, BS8 1TL, UK
[58] Universitäts-Sternwarte München, Fakultät für Physik, Ludwig-Maximilians-Universität München, Scheinerstrasse 1, 81679 München, Germany
[59] FRACTAL S.L.N.E., calle Tulipán 2, Portal 13 1A, 28231, Las Rozas de Madrid, Spain
[60] Max Planck Institute for Extraterrestrial Physics, Giessenbachstr. 1, 85748 Garching, Germany
[61] Dipartimento di Fisica "Aldo Pontremoli", Università degli Studi di Milano, Via Celoria 16, 20133 Milano, Italy
[62] INFN-Sezione di Milano, Via Celoria 16, 20133 Milano, Italy
[63] NRC Herzberg, 5071 West Saanich Rd, Victoria, BC V9E 2E7, Canada
[64] Institute of Theoretical Astrophysics, University of Oslo, P.O. Box 1029 Blindern, 0315 Oslo, Norway
[65] Jet Propulsion Laboratory, California Institute of Technology, 4800 Oak Grove Drive, Pasadena, CA, 91109, USA
[66] Felix Hormuth Engineering, Goethestr. 17, 69181 Leimen, Germany
[67] Technical University of Denmark, Elektrovej 327, 2800 Kgs. Lyngby, Denmark
[68] Cosmic Dawn Center (DAWN), Denmark
[69] Institut d'Astrophysique de Paris, UMR 7095, CNRS, and Sorbonne Université, 98 bis boulevard Arago, 75014 Paris, France
[70] Max-Planck-Institut für Astronomie, Königstuhl 17, 69117 Heidelberg, Germany
[71] NASA Goddard Space Flight Center, Greenbelt, MD 20771, USA

[72] Department of Physics and Helsinki Institute of Physics, Gustaf Hällströmin katu 2, 00014 University of Helsinki, Finland

[73] Leiden Observatory, Leiden University, Einsteinweg 55, 2333 CC Leiden, The Netherlands

[74] Université de Genève, Département de Physique Théorique and Centre for Astroparticle Physics, 24 quai Ernest-Ansermet, CH-1211 Genève 4, Switzerland

[75] Department of Physics, P.O. Box 64, 00014 University of Helsinki, Finland

[76] Helsinki Institute of Physics, Gustaf Hällströmin katu 2, University of Helsinki, Helsinki, Finland

[77] Centre de Calcul de l'IN2P3/CNRS, 21 avenue Pierre de Coubertin 69627 Villeurbanne Cedex, France

[78] Laboratoire d'etude de l'Univers et des phenomenes eXtremes, Observatoire de Paris, Université PSL, Sorbonne Université, CNRS, 92190 Meudon, France

[79] SKA Observatory, Jodrell Bank, Lower Withington, Macclesfield, Cheshire SK11 9FT, UK

[80] University of Applied Sciences and Arts of Northwestern Switzerland, School of Computer Science, 5210 Windisch, Switzerland

[81] Universität Bonn, Argelander-Institut für Astronomie, Auf dem Hügel 71, 53121 Bonn, Germany

[82] INFN-Sezione di Roma, Piazzale Aldo Moro, 2 - c/o Dipartimento di Fisica, Edificio G. Marconi, 00185 Roma, Italy

[83] Dipartimento di Fisica e Astronomia "Augusto Righi" - Alma Mater Studiorum Università di Bologna, via Piero Gobetti 93/2, 40129 Bologna, Italy

[84] Department of Physics, Institute for Computational Cosmology, Durham University, South Road, Durham, DH1 3LE, UK

[85] Université Côte d'Azur, Observatoire de la Côte d'Azur, CNRS, Laboratoire Lagrange, Bd de l'Observatoire, CS 34229, 06304 Nice cedex 4, France

[86] Université Paris Cité, CNRS, Astroparticule et Cosmologie, 75013 Paris, France

[87] CNRS-UCB International Research Laboratory, Centre Pierre Binetruy, IRL2007, CPB-IN2P3, Berkeley, USA

[88] University of Applied Sciences and Arts of Northwestern Switzerland, School of Engineering, 5210 Windisch, Switzerland

[89] Institut d'Astrophysique de Paris, 98bis Boulevard Arago, 75014, Paris, France

[90] Institute of Physics, Laboratory of Astrophysics, Ecole Polytechnique Fédérale de Lausanne (EPFL), Observatoire de Sauverny, 1290 Versoix, Switzerland

[91] Aurora Technology for European Space Agency (ESA), Camino bajo del Castillo, s/n, Urbanizacion Villafranca del Castillo, Villanueva de la Cañada, 28692 Madrid, Spain

[92] Institut de Física d'Altes Energies (IFAE), The Barcelona Institute of Science and Technology, Campus UAB, 08193 Bellaterra (Barcelona), Spain

[93] European Space Agency/ESTEC, Keplerlaan 1, 2201 AZ Noordwijk, The Netherlands

[94] School of Mathematics, Statistics and Physics, Newcastle University, Herschel Building, Newcastle-upon-Tyne, NE1 7RU, UK

[95] DARK, Niels Bohr Institute, University of Copenhagen, Jagtvej 155, 2200 Copenhagen, Denmark

[96] Waterloo Centre for Astrophysics, University of Waterloo, Waterloo, Ontario N2L 3G1, Canada

[97] Department of Physics and Astronomy, University of Waterloo, Waterloo, Ontario N2L 3G1, Canada

[98] Perimeter Institute for Theoretical Physics, Waterloo, Ontario N2L 2Y5, Canada

[99] Université Paris-Saclay, Université Paris Cité, CEA, CNRS, AIM, 91191, Gif-sur-Yvette, France

[100] Centre National d'Etudes Spatiales – Centre spatial de Toulouse, 18 avenue Edouard Belin, 31401 Toulouse Cedex 9, France

[101] Institute of Space Science, Str. Atomistilor, nr. 409 Măgurele, Ilfov, 077125, Romania

[102] Consejo Superior de Investigaciones Científicas, Calle Serrano 117, 28006 Madrid, Spain

[103] Universidad de La Laguna, Departamento de Astrofísica, 38206 La Laguna, Tenerife, Spain

[104] Dipartimento di Fisica e Astronomia "G. Galilei", Università di Padova, Via Marzolo 8, 35131 Padova, Italy

[105] Institut für Theoretische Physik, University of Heidelberg, Philosophenweg 16, 69120 Heidelberg, Germany

[106] Institut de Recherche en Astrophysique et Planétologie (IRAP), Université de Toulouse, CNRS, UPS, CNES, 14 Av. Edouard Belin, 31400 Toulouse, France

[107] Université St Joseph; Faculty of Sciences, Beirut, Lebanon

[108] Departamento de Física, FCFM, Universidad de Chile, Blanco Encalada 2008, Santiago, Chile

[109] Universität Innsbruck, Institut für Astro- und Teilchenphysik, Technikerstr. 25/8, 6020 Innsbruck, Austria

[110] Satlantis, University Science Park, Sede Bld 48940, Leioa-Bilbao, Spain

[111] Infrared Processing and Analysis Center, California Institute of Technology, Pasadena, CA 91125, USA

[112] Instituto de Astrofísica e Ciências do Espaço, Faculdade de Ciências, Universidade de Lisboa, Tapada da Ajuda, 1349-018 Lisboa, Portugal

[113] Cosmic Dawn Center (DAWN)

[114] Niels Bohr Institute, University of Copenhagen, Jagtvej 128, 2200 Copenhagen, Denmark

[115] Universidad Politécnica de Cartagena, Departamento de Electrónica y Tecnología de Computadoras, Plaza del Hospital 1, 30202 Cartagena, Spain

[116] Kapteyn Astronomical Institute, University of Groningen, PO Box 800, 9700 AV Groningen, The Netherlands

[117] Dipartimento di Fisica e Scienze della Terra, Università degli Studi di Ferrara, Via Giuseppe Saragat 1, 44122 Ferrara, Italy

[118] Istituto Nazionale di Fisica Nucleare, Sezione di Ferrara, Via Giuseppe Saragat 1, 44122 Ferrara, Italy

[119] INAF, Istituto di Radioastronomia, Via Piero Gobetti 101, 40129 Bologna, Italy

[120] School of Physics and Astronomy, Cardiff University, The Parade, Cardiff, CF24 3AA, UK

[121] Department of Physics, Oxford University, Keble Road, Oxford OX1 3RH, UK

[122] Université PSL, Observatoire de Paris, Sorbonne Université, CNRS, LERMA, 75014, Paris, France

[123] Université Paris-Cité, 5 Rue Thomas Mann, 75013, Paris, France

[124] Zentrum für Astronomie, Universität Heidelberg, Philosophenweg 12, 69120 Heidelberg, Germany

[125] INAF - Osservatorio Astronomico di Brera, via Emilio Bianchi 46, 23807 Merate, Italy

[126] INAF-Osservatorio Astronomico di Brera, Via Brera 28, 20122 Milano, Italy, and INFN-Sezione di Genova, Via Dodecaneso 33, 16146, Genova, Italy

[127] ICL, Junia, Université Catholique de Lille, LITL, 59000 Lille, France

[128] ICSC - Centro Nazionale di Ricerca in High Performance Computing, Big Data e Quantum Computing, Via Magnanelli 2, Bologna, Italy

[129] Instituto de Física Teórica UAM-CSIC, Campus de Cantoblanco, 28049 Madrid, Spain

[130] CERCA/ISO, Department of Physics, Case Western Reserve University, 10900 Euclid Avenue, Cleveland, OH 44106, USA

[131] Technical University of Munich, TUM School of Natural Sciences, Physics Department, James-Franck-Str. 1, 85748 Garching, Germany

[132] Max-Planck-Institut für Astrophysik, Karl-Schwarzschild-Str. 1, 85748 Garching, Germany

[133] Laboratoire Univers et Théorie, Observatoire de Paris, Université PSL, Université Paris Cité, CNRS, 92190 Meudon, France

[134] Departamento de Física Fundamental. Universidad de Salamanca. Plaza de la Merced s/n. 37008 Salamanca, Spain

[135] Université de Strasbourg, CNRS, Observatoire astronomique de Strasbourg, UMR 7550, 67000 Strasbourg, France

[136] Center for Data-Driven Discovery, Kavli IPMU (WPI), UTIAS, The University of Tokyo, Kashiwa, Chiba 277-8583, Japan

[137] Ludwig-Maximilians-University, Schellingstrasse 4, 80799 Munich, Germany

[138] Max-Planck-Institut für Physik, Boltzmannstr. 8, 85748 Garching, Germany

[139] Dipartimento di Fisica - Sezione di Astronomia, Università di Trieste, Via Tiepolo 11, 34131 Trieste, Italy

[140] California Institute of Technology, 1200 E California Blvd, Pasadena, CA 91125, USA

[141] Department of Physics & Astronomy, University of California Irvine, Irvine CA 92697, USA

[142] Department of Mathematics and Physics E. De Giorgi, University of Salento, Via per Arnesano, CP-I93, 73100, Lecce, Italy

[143] INFN, Sezione di Lecce, Via per Arnesano, CP-193, 73100, Lecce, Italy

[144] INAF-Sezione di Lecce, c/o Dipartimento Matematica e Fisica, Via per Arnesano, 73100, Lecce, Italy

[145] Departamento Física Aplicada, Universidad Politécnica de Cartagena, Campus Muralla del Mar, 30202 Cartagena, Murcia, Spain

[146] Instituto de Física de Cantabria, Edificio Juan Jordá, Avenida de los Castros, 39005 Santander, Spain

[147] CEA Saclay, DFR/IRFU, Service d'Astrophysique, Bat. 709, 91191 Gif-sur-Yvette, France

[148] Institute of Cosmology and Gravitation, University of Portsmouth, Portsmouth PO1 3FX, UK

[149] Department of Astronomy, University of Florida, Bryant Space Science Center, Gainesville, FL 32611, USA

[150] Department of Computer Science, Aalto University, PO Box 15400, Espoo, FI-00 076, Finland

[151] Instituto de Astrofísica de Canarias, c/ Via Lactea s/n, La Laguna 38200, Spain. Departamento de Astrofísica de la Universidad de La Laguna, Avda. Francisco Sanchez, La Laguna, 38200, Spain

[152] Caltech/IPAC, 1200 E. California Blvd., Pasadena, CA 91125, USA

[153] Ruhr University Bochum, Faculty of Physics and Astronomy, Astronomical Institute (AIRUB), German Centre for Cosmological Lensing (GCCL), 44780 Bochum, Germany

[154] Department of Physics and Astronomy, Vesilinnantie 5, 20014 University of Turku, Finland

[155] Serco for European Space Agency (ESA), Camino bajo del Castillo, s/n, Urbanizacion Villafranca del Castillo, Villanueva de la Cañada, 28692 Madrid, Spain

[156] ARC Centre of Excellence for Dark Matter Particle Physics, Melbourne, Australia

[157] Centre for Astrophysics & Supercomputing, Swinburne University of Technology, Hawthorn, Victoria 3122, Australia

[158] Department of Physics and Astronomy, University of the Western Cape, Bellville, Cape Town, 7535, South Africa

[159] DAMTP, Centre for Mathematical Sciences, Wilberforce Road, Cambridge CB3 0WA, UK

[160] Kavli Institute for Cosmology Cambridge, Madingley Road, Cambridge, CB3 0HA, UK

[161] Department of Astrophysics, University of Zurich, Winterthurerstrasse 190, 8057 Zurich, Switzerland

[162] Department of Physics, Centre for Extragalactic Astronomy, Durham University, South Road, Durham, DH1 3LE, UK

[163] IRFU, CEA, Université Paris-Saclay 91191 Gif-sur-Yvette Cedex, France

[164] Oskar Klein Centre for Cosmoparticle Physics, Department of Physics, Stockholm University, Stockholm, SE-106 91, Sweden

[165] Astrophysics Group, Blackett Laboratory, Imperial College London, London SW7 2AZ, UK

[166] Univ. Grenoble Alpes, CNRS, Grenoble INP, LPSC-IN2P3, 53, Avenue des Martyrs, 38000, Grenoble, France

[167] INAF-Osservatorio Astrofisico di Arcetri, Largo E. Fermi 5, 50125, Firenze, Italy

[168] Dipartimento di Fisica, Sapienza Università di Roma, Piazzale Aldo Moro 2, 00185 Roma, Italy

[169] Centro de Astrofísica da Universidade do Porto, Rua das Estrelas, 4150-762 Porto, Portugal

[170] Dipartimento di Fisica, Università di Roma Tor Vergata, Via della Ricerca Scientifica 1, Roma, Italy

[171] INFN, Sezione di Roma 2, Via della Ricerca Scientifica 1, Roma, Italy

[172] HE Space for European Space Agency (ESA), Camino bajo del Castillo, s/n, Urbanizacion Villafranca del Castillo, Villanueva de la Cañada, 28692 Madrid, Spain

[173] Department of Astrophysical Sciences, Peyton Hall, Princeton University, Princeton, NJ 08544, USA

[174] Theoretical astrophysics, Department of Physics and Astronomy, Uppsala University, Box 515, 751 20 Uppsala, Sweden

[175] Mathematical Institute, University of Leiden, Einsteinweg 55, 2333 CA Leiden, The Netherlands

[176] School of Physics & Astronomy, University of Southampton, Highfield Campus, Southampton SO17 1BJ, UK

[177] Institute of Astronomy, University of Cambridge, Madingley Road, Cambridge CB3 0HA, UK

[178] Department of Physics and Astronomy, University of California, Davis, CA 95616, USA

[179] Space physics and astronomy research unit, University of Oulu, Pentti Kaiteran katu 1, FI-90014 Oulu, Finland

[180] Center for Computational Astrophysics, Flatiron Institute, 162 5th Avenue, 10010, New York, NY, USA

[181] Department of Astronomy, University of Massachusetts, Amherst, MA 01003, USA

[182] Univ. Lille, CNRS, Centrale Lille, UMR 9189 CRIStAL, 59000 Lille, France

[183] Department of Physics and Astronomy, University of British Columbia, Vancouver, BC V6T 1Z1, Canada
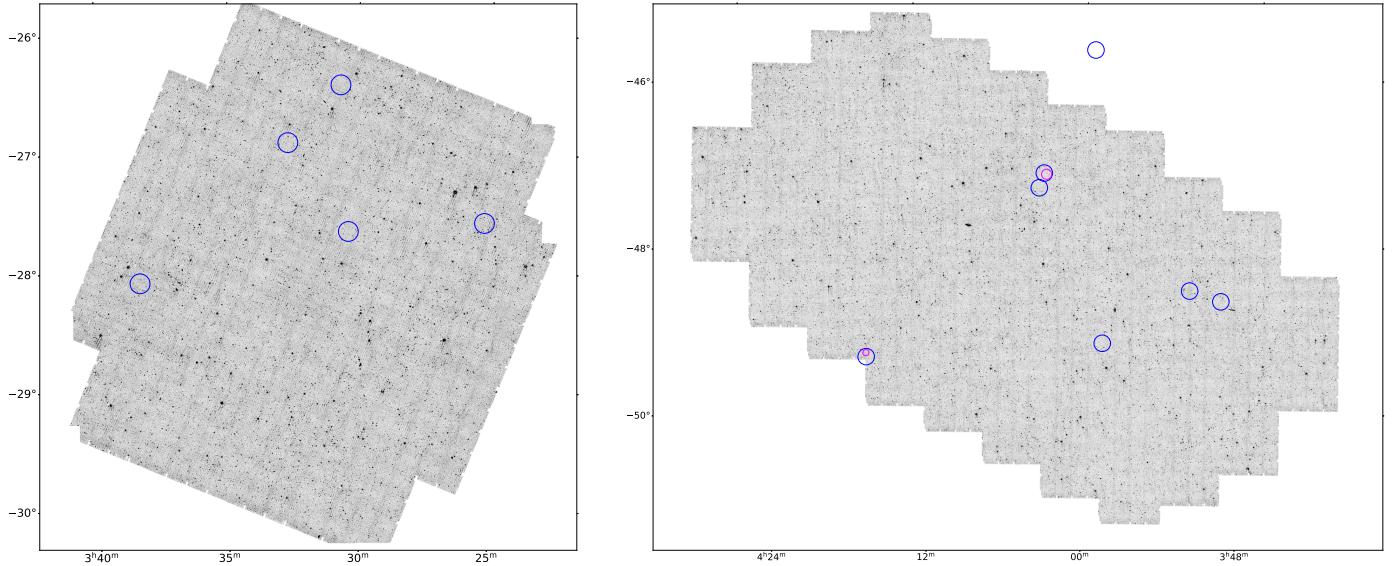
Fig. A.1. *Euclid* EDF-F (left) and *Euclid* EDF-S (right) VIS images, with the *Planck* protocluster candidates shown in blue and the *Euclid* counterparts in magenta.

Appendix A: *Euclid* VIS images of the Q1 EDF-S and EDF-F with the *Planck* protocluster candidates

In this section, we show in Fig. A.1 the *Euclid* VIS images of the EDF-F and EDF-S fields, with the locations indicated for the *Planck* protocluster candidates and the *Euclid* counterparts.